







Article

Floating TiO₂-Cork Nano-Photocatalysts for Water Purification Using Sunlight

Maria Leonor Matias ¹, Maria Morais ¹, Ana Pimentel ¹, Francisco X. Vasconcelos ¹, Ana S. Reis Machado ², Joana Rodrigues ³, Elvira Fortunato ¹, Rodrigo Martins ^{1,*} and Daniela Nunes ^{1,*}

¹ CENIMAT | i3N, Department of Materials Science, School of Science and Technology, NOVA University Lisbon and CEMOP/UNINOVA, 2829-516 Caparica, Portugal

² LAQV-REQUIMTE, Department of Chemistry, NOVA School of Science and Technology, Universidade NOVA de Lisboa, Campus de Caparica, 2829-516 Caparica, Portugal

³ Physics Department and I3N, Aveiro University, Campus Universitário de Santiago, 3810-193 Aveiro, Portugal

* Correspondence: rm@uninova.pt (R.M.); daniela.gomes@fct.unl.pt (D.N.); Tel.: +351-21-294-8562 (R.M. & D.N.); Fax: +351-21-294-8558 (R.M. & D.N.)

Abstract: In the present study, titanium dioxide (TiO₂) nano-photocatalysts were synthesized through microwave irradiation. In a typical microwave synthesis, TiO₂ nanomaterials were simultaneously produced in powder form and also directly covering cork substrates. The TiO₂ nanopowder was analyzed by X-ray diffraction (XRD), Raman spectroscopy and transmission electron microscopy (TEM), revealing that the solvothermal microwave synthesis resulted only in the TiO₂ anatase phase. From Fourier-transform infrared spectroscopy (FTIR), cork's organic species, along with bands of TiO₂, were detected. UV-VIS absorption spectrum revealed an absorption extension to the visible region, since a brown powdered TiO₂ product was obtained. Very fine nanoparticles were observed displaying a nearly spherical shape that agglomerates in larger particles. These larger particles fully covered the surface of the honeycomb cork cells, originating TiO₂ functionalized cork platforms. The TiO₂ functionalized substrates were further tested as floating photocatalysts and their photocatalytic activity was assessed from rhodamine B degradation under solar simulating light and natural sunlight. Reusability tests were also performed under natural sunlight. The strategy applied in this research work allowed the production of green and low-cost cork platforms based on TiO₂ photoactive materials with the ability to purify polluted water under natural sunlight.

Keywords: TiO₂; photocatalysis; water purification; microwave synthesis; floating catalysts; cork



Citation: Matias, M.L.; Morais, M.; Pimentel, A.; Vasconcelos, F.X.; Reis Machado, A.S.; Rodrigues, J.; Fortunato, E.; Martins, R.; Nunes, D. Floating TiO₂-Cork Nano-Photocatalysts for Water Purification Using Sunlight. *Sustainability* **2022**, *14*, 9645. <https://doi.org/10.3390/su14159645>

Academic Editor: Asterios Bakolas

Received: 29 June 2022

Accepted: 2 August 2022

Published: 5 August 2022

Publisher's Note: MDPI stays neutral with regard to jurisdictional claims in published maps and institutional affiliations.



Copyright: © 2022 by the authors. Licensee MDPI, Basel, Switzerland. This article is an open access article distributed under the terms and conditions of the Creative Commons Attribution (CC BY) license (<https://creativecommons.org/licenses/by/4.0/>).

1. Introduction

The rapid development of industrialization and population growth have strongly contributed to the shortage of available clean water, thus increasing the demand for reliable and accessible solutions that enable water purification [1]. The uncontrolled discharge of toxic contaminants into the environment, which include organic pollutants, heavy metals, inorganic compounds, and other complex compounds, has significantly contributed to water contamination [2–4].

In this regard, significant research has been carried out to find economically viable and efficient solutions to face the issue of water pollution. Textile industries significantly contribute to this problem since around 60 thousand tons of textile dyes are discharged annually into the environment [5]. These textile dyes do not bind tightly to fabric, and, consequently, due to their high recalcitrance, they impair photosynthesis, inhibit plant growth, and enter the food chain, endangering animals and plants while promoting toxicity, mutagenicity, and carcinogenicity [6].

Among the most used methods for the treatment of pollutants and remediation of water, adsorption and membrane technologies, as well as biological treatments and advanced oxidation methods, appear as effective treatment methods for wastewater or water sources.

When it comes to adsorption, it is a process that involves the mass transfer of components, where the adsorbents are used to adsorb pollutants (adsorbate) from polluted water with the assistance of intermolecular forces. In the case of membrane technology, it associates biological (membrane bioreactors) with nonbiological processes (ultrafiltration, nanofiltration, among others) to remove pollutants. This technology is now a leading process to achieve relatively clean water from wastewater through the combination of membrane and biological treatments. Regarding the biological treatments, they consist of two types of processes, i.e., activated sludge process and trickling filter. The presence of aerobic bacteria and other microorganisms is imperative to oxidize or incorporate into cells of organic matter. Moreover, the bacteria need enough oxygen for the treatment to occur. After both biological processes, the dense microbial biomass is separated from water by secondary sedimentation. The advanced oxidation methods include ozone, O_3/H_2O_2 , H_2O_2/UV , Fenton, ultrasound, photocatalytic, and electrochemical oxidation [7–9]. Nevertheless, the use of green and cost-effective technologies for the treatment of pollutants and remediation of water, such as in photocatalysis, particularly making full use of the abundance of solar energy, is therefore of utmost importance [10–12].

Different materials and, more frequently, metal oxide semiconductors have been studied for the development of efficient photocatalysts, including WO_3 [13], Fe_2O_3 [14], ZrO_2 [15], $SrTiO_3$ [16], ZnO [17,18] and TiO_2 [19–24]. Among these semiconductors, TiO_2 has been extensively studied for photocatalysis since it is the most promising material for industrial use [25], due to its physical and chemical stabilities, low-cost, non-toxicity and strong oxidation potential to decompose organic pollutants [20,26–29]. Photocatalytic reactions in the presence of TiO_2 mainly consist of three steps: (i) the generation of electron-hole pairs with photon energy superior to its band gap, (ii) migration of electrons and holes to the surface of TiO_2 , and (iii) their reaction with adsorbed electron acceptors and donors, respectively [30]. It is well known that TiO_2 mainly absorbs in the UV region ($\lambda < 387$ nm), which only represents around 5% of the solar spectrum [31], while 43% of the solar spectrum corresponds to the visible region [32]. Despite this drawback, several attempts have successfully been made to extend the light harvesting of TiO_2 to the visible range, including doping with metal and non-metal elements, surface modification and coupling with other semiconductor materials [28,32–34].

The photocatalytic performance of metal oxide semiconductors is strongly dependent on the physical properties of these materials, such as the crystal and electronic structure, morphology, particle size, elemental composition and crystalline phase, as well as the operating conditions, such as the light intensity, amount of photocatalyst and pH of the pollutant media [28,35]. Additionally, it is well known that for metal oxide semiconductors, a decrease in the particle size at the nanoscale leads to an enhancement of their photocatalytic performance due to their higher surface-to-volume ratio [28,36,37]. The excellent photocatalytic properties of these nano-sized materials have also been exhibited under natural sunlight [38,39].

Several chemical and physical methods have been employed for the synthesis of TiO_2 -based materials, including sol-gel [40,41], atomic layer deposition [42], electrospinning, anodization [43], sputtering [44], hydrothermal/solvothermal production methods, including hydrothermal/solvothermal assisted by microwave irradiation [45–47]. Among these methods, microwave irradiation has proven to be a promising alternative, since it is cost-effective, provides accurate temperature/pressure controls with efficient heating of solvents and/or reagents, while maintaining higher yields with a reduced processing time, in addition to the possibility of scale-up for industrial applications [45,48,49].

Over the last few years, a new category of photocatalysts, the “floating photocatalysts”, has emerged with great potential to overcome the issue of recovery and recyclability of nanopowders. The benefits of using floating photocatalysts include flexibility and lightness, while their “floating” characteristic offers the advantages of maximizing the utilization of light, as well as the oxygenation of the photocatalyst due to the proximity of the air/water interface. Moreover, they are easy to collect from water and do not need

complex experimental equipment or stirring during the photocatalytic reaction. Under these circumstances, an optimization of illumination and oxygenation should, hence, improve the radical formation rate and oxidation efficiency [50,51].

In terms of natural floating materials, cork presents several advantages, which makes it suitable in photocatalytic experiments, such as earth-abundance, compressibility, resilience, thermal stability and corrosion resistance, low density [52], non-toxicity and hydrophobicity [50]. Cork is extracted from the bark of the cork oak tree (*Quercus suber* L.) which flourishes in the specific regions of the Western Mediterranean (Portugal, Spain, Southern France, part of Italy, and North Africa) [53], and by being sustainable and renewable [52], it has become a valuable material. As proof of its sustainability, each time the bark is harvested from cork trees, these latter ones can absorb up to 5 times more CO₂ (with the aim of generating their bark) than a non-harvested tree [54]. Moreover, cork contributes to the circular economy, being extracted without damaging the tree and being regenerated over the years, besides being the base of several products, some of them produced by recycled cork [55]. In terms of cork's composition, it depends on several factors, such as geographic origin, climate and soil conditions, tree dimensions, age, among others. However, it is essentially composed by hydrophobic polymers such as suberin (which is mainly responsible for the elasticity and compressibility of cork representing ~46% [56]) and lignin (~27% [56]), as well as by the hydrophilic polysaccharides (~12%), cellulose and hemicellulose [53,57], and extractives (~15% [58]) [2], s waxes and tannins [59].

Portugal is the world's largest producer of cork, with an estimated annual production of around 100 thousand tons. The Cork industry, despite being one of the most profitable markets in the country, generates a large amount of cork that has no commercial value, being usually burnt to generate energy [54]. The combination of green advanced materials and technology, which can tackle issues of sustainability, such as water pollution, has to be adopted for a sustainable future [60]. Hence, instead of wasting cork and to take advantage of its unique properties, it could serve as a platform in photocatalytic applications for the treatment of contaminated effluents, which would valorize both the cork industry and the effluent treatment industry.

Studies focused on the production of TiO₂-based materials on cork and the investigation of their photocatalytic efficiency are scarce, and to the best of our knowledge, the synthesis of nano-TiO₂ photocatalysts on cork by a fast and low temperature microwave synthesis has never been reported. Regarding the previous studies, Sboui et al. reported the preparation of TiO₂-Polyaniline (PANI) nanocomposites for the degradation of methyl orange (MO) dye by using a sol-gel method for the synthesis of TiO₂ nanostructures, followed by an additional step to immobilize the nanocomposite on cork surface [50]. In another study, TiO₂/polyvinyl alcohol (PVA)/Cork nanocomposites were prepared through the immobilization of TiO₂ nanoparticles on cork and by employing PVA as a binder to anchor TiO₂ nanoparticles on the surface of the floating catalyst for the degradation of methylene blue (MB) [61]. For the photocatalyst preparation, several steps were involved, and higher temperatures were required to calcinate the TiO₂ nanostructures.

Therefore, in this work, pure TiO₂ photocatalysts were synthesized on cork substrates by a fast and low temperature single step solvothermal method under microwave irradiation (120 °C for 1 h). The produced materials (nanopowder and/or functionalized substrates) were systematically characterized by XRD, Raman spectroscopy, FTIR, SEM coupled with EDS, and TEM. The optical properties were assessed through UV-VIS absorption measurements. Finally, the photocatalytic activity of the TiO₂ functionalized cork platforms was evaluated from the evolution of rhodamine B (RhB) degradation under solar simulated light and natural sunlight.

2. Experimental Procedure

Synthesis of TiO₂ Nanostructures on Cork via Microwave Irradiation

Titanium (IV) isopropoxide (TTIP) with 97% purity from Sigma-Aldrich, St. Louis, MO, USA (CAS: 546-68-9) was used as the titanium dioxide precursor. To prepare a solution

of 120 mL, 10 mL of a 1 M acid solution (oxalic acid anhydrous from Sigma-Aldrich (CAS: 144-62-7) was added to 110 mL of absolute anhydrous ethanol from Carlo Erba reagents, Val-de-Reuil, France (CAS: 64-17-5) and stirred for 10 min, until a homogeneous solution was obtained. Afterwards, 4 mL of TTIP was added dropwise to the previous solution. Then, the obtained solution was left to stir overnight. This process guarantees the complete homogenization of the solution. Microwave synthesis was performed using a CEM microwave digestion system, Matthews, NC, USA (MARS one) and was carried out at 1000 W, 120 ± 10 °C for 1 h. Solution volumes of 20 mL were transferred into Teflon vessels of 75 mL, which were kept sealed. To produce the functionalized cork platforms, cork sheets with a thickness of 2 mm from Bi-Office (ref. RL044330 222468) were cut into pieces of 1.5×3.5 cm², fixed with Kapton tape to ordinary glass squares and each cork piece was transferred to individual microwave vessels containing the solution. Each piece should be completely in contact with the solution. The functionalized cork platforms were afterwards cleaned in an ultrasonic bath, first with deionized water for 10 min and then with isopropyl alcohol (IPA) for another 10 min. To remove the excess solvents from the cork substrates, each piece was left to dry for a few minutes on top of lab paper and dried at 60 °C in a desiccator between 30 min and 2 h. TiO₂ nanopowder was simultaneously formed during microwave synthesis. The nanopowder was washed repeatedly several times with deionized water, followed by isopropyl alcohol (IPA), using a centrifuge at 4500 rpm for 5 min each time. Finally, the nanopowder was kept overnight in a desiccator for drying at 80 °C in vacuum. For comparison, a microwave synthesis was carried out without the cork substrates, and pure TiO₂ nanopowder was obtained by using the same experimental conditions as the TiO₂ nanopowder produced in the presence of cork substrates. A schematic of the experimental procedure is shown in Figure 1.

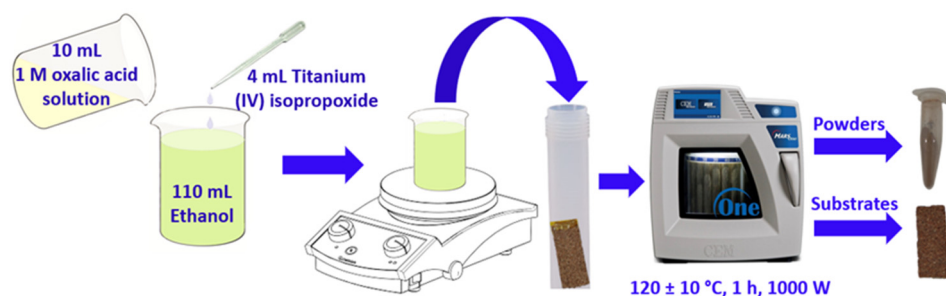


Figure 1. Scheme of the TiO₂ microwave synthesis procedure. The real images of the cork substrates before and after synthesis are shown together with the TiO₂ nanopowder simultaneously produced.

It should be noted that the final functionalized cork exhibited a slightly darker color after microwave synthesis. This has also been previously reported owing to an increase in temperature, assigned to the reactions of the extractives, without any degradation associated [62].

3. Characterization Techniques

XRD experiments were performed using a PANalytical's X'Pert PRO MPD diffractometer (Almelo, The Netherlands) equipped with a X'Celerator 1D detector and using CuK α radiation ($\lambda = 1.540598$ Å). XRD data were recorded from 20° to 80° 2 θ range with a step of 0.05°. The TiO₂ powder, pristine cork and functionalized cork substrates were measured. The simulated brookite corresponds to ICDD file No. 00-029-1360, simulated rutile to ICSD file No. 00-021-1276 and the simulated anatase to ICSD file No.00-21-1272 with $a = b = 3.7852$ Å and $c = 9.5139$ Å. The average crystallite size of the synthesized nano-materials was estimated by the Debye–Scherrer equation [63] using the software X'pert highscore plus (Almelo, The Netherlands, version 4.6a (4.6.1.23823) [64] for the most intense peak, reflection (101) [65,66].

SEM images were obtained using a Hitachi Regulus 8220 Scanning Electron Microscope (Mito, Japan), while for the energy dispersive X-ray spectroscopy (EDS) analyses, a Carl Zeiss AURIGA CrossBeam FIB-SEM workstation (Oberkochen, Germany) was used.

TEM observations were carried out with a Hitachi HF5000 field-emission transmission electron microscope operated at 200 kV (Mito, Japan). A drop of the sonicated dispersion was deposited onto 200-mesh copper grids covered with formvar and allowed to dry before observation. The average particle size and standard deviation were calculated from the dimensions of several nanoparticles (30 measurements) based on TEM images. Image J software was used to measure the nanoparticles. The absorption measurements were carried out using a Perkin Elmer lambda 950 UV/VIS/NIR spectrophotometer (Waltham, MA, USA) and the measurements were performed in the 250–800 nm range.

Raman spectroscopy measurements were obtained with an inVia Qontor confocal Raman microscope from Renishaw (Kingswood, UK). A 50 mW green diode pumped solid state laser operated at 532 nm was used as the excitation source, with a 10 s exposure time and settings of 3 accumulations. The Raman spectra were recorded as an extended scan in the range of 100–700 cm^{-1} . The laser beam was focused with a long working distance (8.2 mm) 50 \times Olympus objective. The results present are based on the average of several scans taken on the surface of the synthesized nanopowder and cork substrates. The 521 cm^{-1} peak of a silicon wafer was used to calibrate the spectrograph for possible fluctuations of the Raman system. All measurements were performed at RT.

FTIR transmittance spectrum of the produced powders was recorded on a Perkin-Elmer FT-IR Spectrometer Spectrum Two (Waltham, MA, USA), equipped with an attenuated total reflection (ATR) cell in the range of 400–4000 cm^{-1} . The measurements were performed at RT.

3.1. Photocatalytic RhB Degradation under Solar Simulating Light

The photocatalytic activity of TiO_2 on cork was evaluated at RT considering the degradation of RhB ($\text{C}_{28}\text{H}_{31}\text{ClN}_2\text{O}_3$) from Sigma-Aldrich. The TiO_2 nanomaterials were synthesized directly on cork substrates to avoid the recovery of nanosized materials in powder form. All the experiments were performed according to the international standard ISO 10678 [45]. For each experiment, cork pieces were placed on the reaction recipient and before the reaction, the catalysts and the dye solution (50 mL of the RhB solution (5 mg/L)) were kept in the dark for 1 h to establish absorption–desorption equilibrium. No stirring was used during the reactions to avoid oxygenation of the solution and to simulate the use of a floating photocatalyst [50]. Solar light exposure was carried out by using a light-emitting diode (LED) solar simulator LSH 7320 (AM 1.5 spectrum) with an intensity of 100 mW/cm^2 (1000 W/m^2). Absorption spectra were recorded using a PerkinElmer lambda 950 UV/VIS/NIR spectrophotometer with different time intervals up to a total of 12 h. The measurements were performed in the 400–700 nm range. The blank RhB solution and pristine cork substrate were also exposed with identical conditions.

3.2. Photocatalytic RhB Degradation under Natural Sunlight

RhB photocatalytic degradation under natural sunlight was monitored around midday in the city of Caparica and in the month of May. The total exposure time was 4 h, since after that time (at the end of the day) the solar intensity significantly decreased. Moreover, if the exposure was continued on another day, the experimental conditions (solar intensity and UV level) would significantly differ, and for that reason, it has been considered 4 h of sunlight exposure for each photocatalytic experiment.

The sunlight intensity was measured three times by using a solar power meter from Sciencetech (Sciencetech-Inc., London, ON, Canada): before light exposure, in the middle and at the end of the experiment. Reusability tests were also performed with the functionalized cork substrates for the RhB degradation under three consecutive cycles and up to 4 h. These experiments consisted of recovering the cork substrates with further discard of the total liquid. The recovered cork pieces were dried in air prior to the next

exposure. After that, the recovered materials were poured into a fresh solution and exposed to light considering the same exposure times. The pristine substrate was also exposed for comparison. Before light exposure, the sunlight intensity was 810, 800 and 880 W/m², respectively, for the first, second and third experiments. In the middle of the experiments (after 2 h of light exposure), the intensity decreased to 730, 750 and 810 W/m², respectively, for the first, second and third experiments. At the end of the experiments (after 4 h of light exposure), the sunlight intensity was 400, 350 and 300 W/m², respectively, for the first, second and third experiments. During the photocatalysis experiments, the temperatures were between 17–26 °C, 19–28 °C and 20–26 °C in the first, second and third experiments, respectively. The UV levels were 7 out of 11 in the first experiment and 8 out of 11 in the second and third experiments, according to IPMA (Instituto Português do Mar e da Atmosfera) website [67].

4. Results and Discussion

Microwave synthesis was successfully used to produce TiO₂ nanopowders and also to synthesize TiO₂ nanostructures directly on cork substrates. The syntheses were carried out using oxalic acid at low temperatures (120 °C) for 1 h and without any seed layer or preliminary preparation step. The TiO₂ nanopowder, as well as the TiO₂ functionalized cork platforms, were systematically investigated, and the cork-based materials were tested as floating photocatalysts.

4.1. Structural and Optical Characterization of the TiO₂ Nanopowder

4.1.1. X-ray Diffraction

Figure 2 shows the experimental XRD diffractogram of the TiO₂ nanopowder. All experimental peaks are fully assigned to TiO₂ tetragonal anatase phase (JCPDS 21-1272), and correspond to the reflections (101), (004), (200), (105), (211), (204), (116), (220) and (215) at $2\theta = 25.3, 37.8, 48.0, 53.8, 54.9, 62.8, 68.9$ and 75.0° , respectively. No peaks related to other TiO₂ crystalline phases (brookite or rutile) were observed. Moreover, no impurities were detected, such as Ti(OH)₄ [45,68]. The XRD results also demonstrate that the materials are well crystallized and the broad diffraction peaks indicate the presence of very small sized crystallites [45,68]. Some contribution from the cork's chemical components released during synthesis, especially due to the brown color of the resulting powders, was expected. However, it was not confirmed by the XRD results.

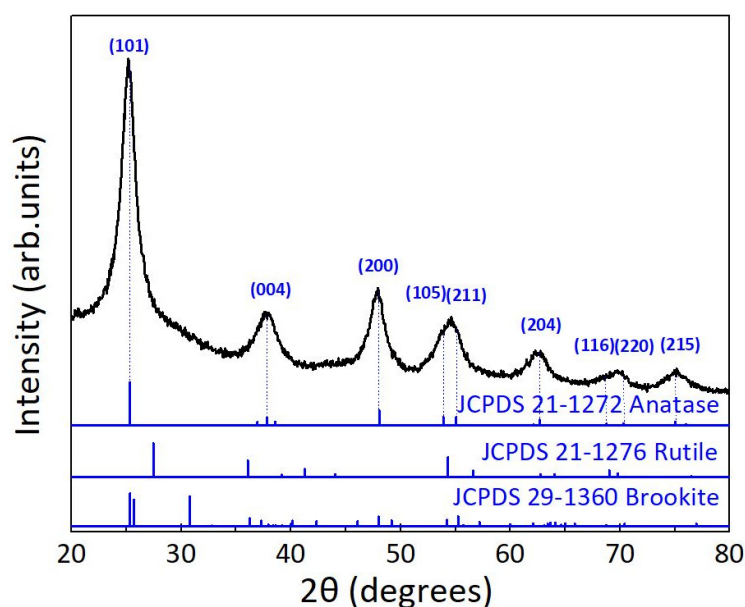


Figure 2. XRD diffractogram of TiO₂ nanopowder simultaneously synthesized by microwave irradiation. For comparison, the simulated TiO₂ anatase, rutile and brookite structures are also presented.

The average crystallite size of the synthesized TiO₂ nanomaterials was obtained by using the Scherrer equation. The calculated crystallite size value was found to be around 4.8 nm.

4.1.2. Raman Spectroscopy Measurements

Raman spectroscopy measurements were performed to confirm the purity of the synthesized materials. Since the cork substrates obscured the signal of the TiO₂ nanomaterials (see Figure S1), probably due to the high penetration depth of the laser's light (in this case with a wavelength of 532 nm), only the materials in powder form were investigated. It can be observed from the Raman spectrum in Figure 3 that the five typical TiO₂ anatase bands appear at 144 cm⁻¹ (E_g), 198 cm⁻¹ (E_g), 393 cm⁻¹ (B_{1g}), 515 cm⁻¹ (B_{1g} + A_{1g}) and 636 cm⁻¹ (E_g) [68,69] with the six Raman active modes (A_{1g} + 2B_{1g} + 3 E_g) [70]. The purity of the produced TiO₂ nanopowder is thus confirmed and corroborates with the XRD data.

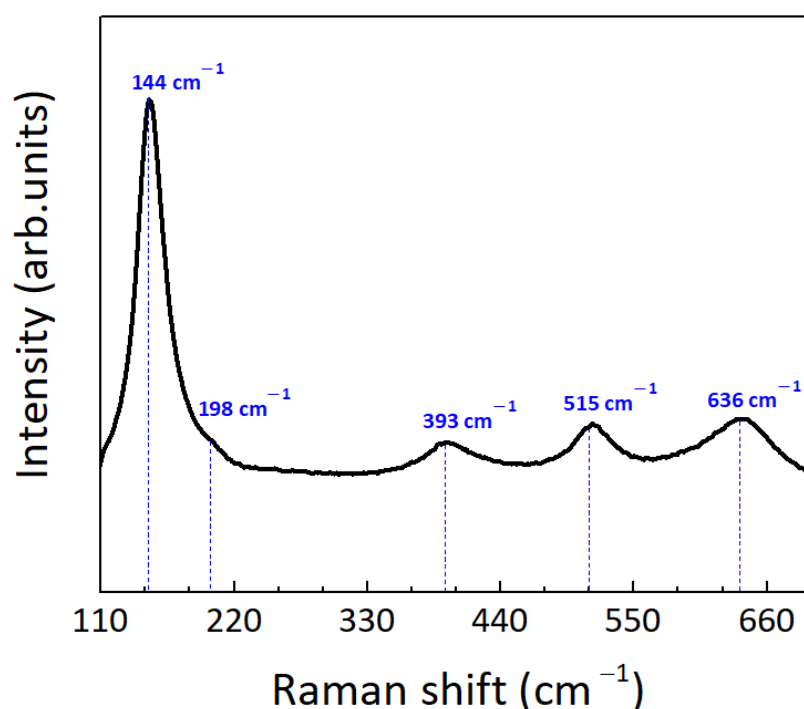


Figure 3. Representative Raman spectrum of the synthesized TiO₂ nanopowder. The vertical dot lines represent anatase TiO₂ bands.

4.1.3. FTIR

The TiO₂ nanopowder was also investigated using FTIR and the result is presented in Figure 4. The appearance of a broad band between 3000 and 3600 cm⁻¹, as well as the band at 1680 cm⁻¹, indicates the presence of hydroxyl groups, due to the adsorption of water from the surrounding environment [43,50,71,72]. For the lower wavenumber region, a peak located at around 1111 cm⁻¹ is visible and attributed to the stretching vibration of the Ti-OH bond [50], whereas the peaks located at 438 cm⁻¹ and 1396 cm⁻¹ are attributed to Ti-O bending [73] and Ti-O-Ti stretching modes [74], respectively. Other peaks corresponding to vibrational modes of residual organic species were also observed. FTIR stretching band at 1680 cm⁻¹ is likely related to C=O groups [75,76], while the broad and small peak that appears at 1260 cm⁻¹ is probably ascribed to C-O stretching mode from groups such as ethers (common linkages in lignin [77]), alcohols, esters, lactones, phenols or carboxylic acids [78], all present in cork's chemical composition [79–81].

The brown nanopowder obtained from microwave synthesis may indicate the presence of organic species coming from the cork substrates (see Figure 1), as revealed by FTIR, and not detected by XRD and Raman spectroscopy techniques. Nevertheless, anatase TiO₂

phase was obtained, as seen previously from the XRD and Raman spectroscopy results, indicating the successful conversion of the TiO_2 precursors under microwave irradiation, which is based on the following Equations (1) and (2) [82]:

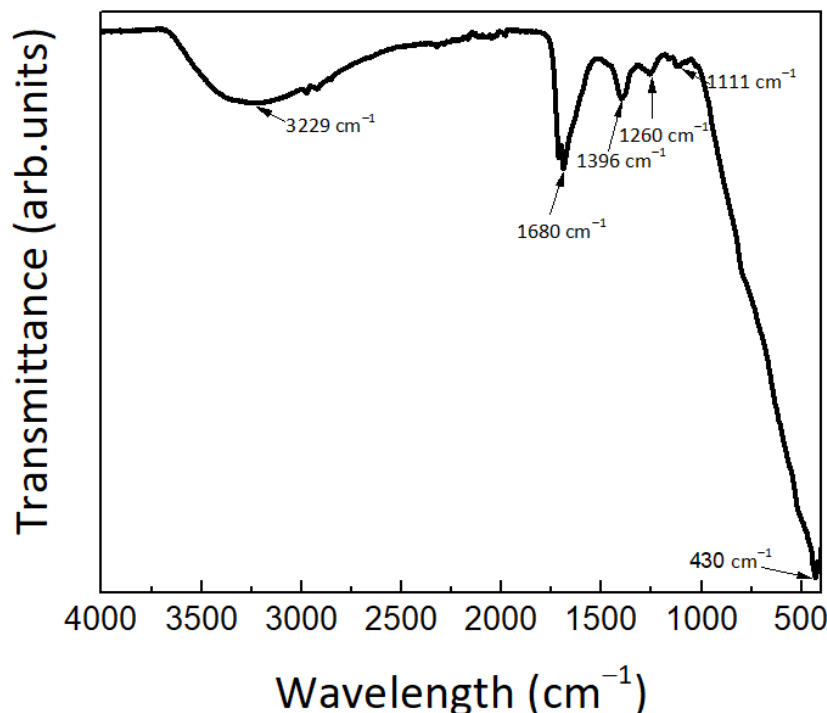
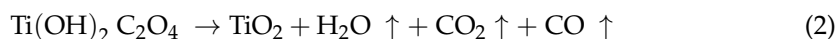
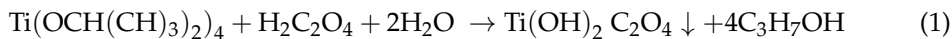


Figure 4. FTIR spectrum of the TiO_2 nanopowder.

4.1.4. Electron Microscopy

Figure 5 shows the SEM and TEM images of the TiO_2 nanopowder synthesized under microwave irradiation. From the SEM image (Figure 5a), it can be observed the formation of nano-sized particles largely agglomerated. Nevertheless, from TEM, it could be perceived that these agglomerates are formed by very fine nanoparticles, displaying a nearly spherical shape (Figure 5c,d). The average particle size was found to be 4.86 ± 1.31 nm. The inset in Figure 5b also shows the particle size distribution, revealing that smaller particles in the range of 4–6 nm are more likely to be found. The ring diffraction pattern in Figure 5b attested that these particles are solely from the anatase phase. Moreover, the fast Fourier transform (FFT) images and the lattice spacing (~ 0.35 nm) correspond to the (101) planes of anatase TiO_2 nanocrystals, Figure 5c,d. From the FFT image in Figure 5c, taken in the area indicated as A in the black square, it can be observed that two sets of lattices are present and that they are not perpendicular to each other with an equal lattice spacing of ~ 0.35 nm, corresponding to the (101) and (011) planes of the anatase phase. Observed through the $[11\bar{1}]$ zone axis, the angle inferred between both (101) and (011) is 82° in accordance with the theoretical value reported for pure TiO_2 anatase (JCPDS 21-1272).

The TiO_2 nanopowder synthesized without cork substrates was also observed by SEM (Figure S2), revealing that, as observed for the TiO_2 nanopowder synthesized with cork substrates, the microwave synthesis resulted in very fine nanoparticles, in agreement with an analogous study [23].

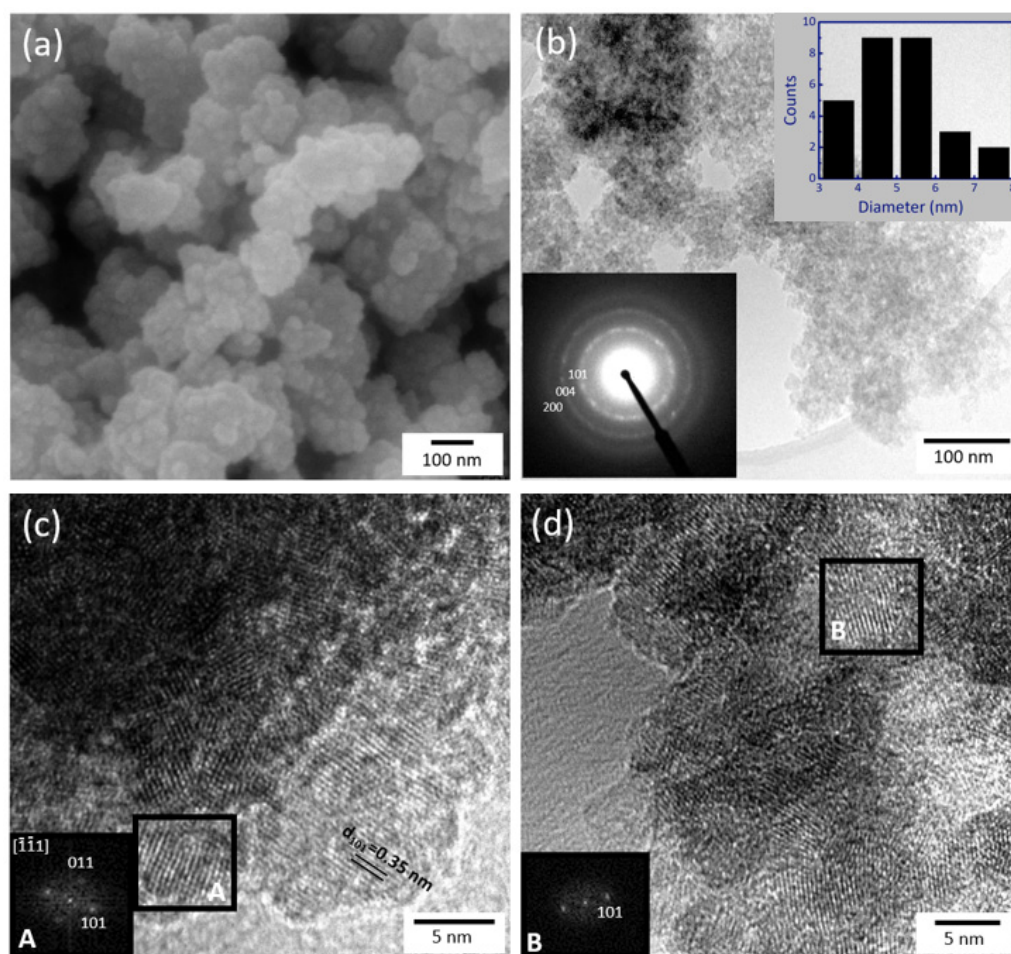


Figure 5. (a) SEM image of the TiO₂ nanopowder synthesized under microwave irradiation (120 °C for 1 h). TEM images of the TiO₂ nanopowder: (b) bright-field image of the TiO₂ nanopowder, (c,d) high resolution TEM image of the nanocrystals. The insets in (b) depict the electron diffraction pattern of TiO₂ nanoparticles with the anatase phase together with the particle size distribution, and (c,d) show the FFT images of the areas indicated as A and B, respectively (black squares).

4.1.5. Optical Characterization

The optical properties of the produced TiO₂ nanopowder (in the presence of the cork substrates) were investigated by recording the UV–VIS absorption spectrum (see Figure 6). As observed in Figure 6, an absorption maximum is obtained in the UV region, around 306 nm (~4.1 eV), and the absorption is seen to extend throughout the visible region. For comparison, the absorption spectrum of the TiO₂ nanopowder synthesized in the absence of the cork substrates was also recorded (Figure S2). In this last case, even though the absorption maximum is placed at the same value as in Figure 6, no absorption occurs beyond 400 nm as expected, since pure TiO₂ presents a wide band gap value (around 3.2 eV for pure TiO₂ anatase nanoparticles [45,83,84]). It can thus be concluded that the visible light absorption in Figure 6 may be attributed to the presence of binders that were transferred from the cork during microwave synthesis and resulted in brown TiO₂ nanopowders. In fact, several studies have reported the impact of different binders on the TiO₂ nanostructures, with these extractives interacting with the nanostructures and modifying their morphology, size and optical properties [85–87].

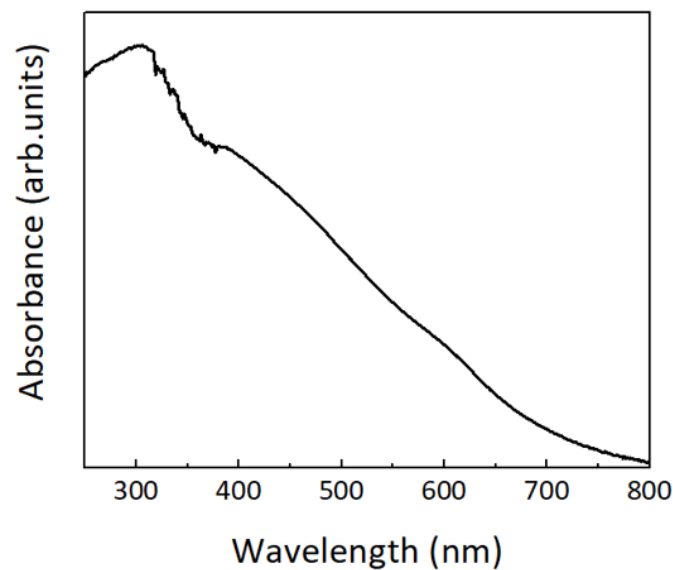


Figure 6. Absorption curve of the TiO₂ nanopowder synthesized under microwave irradiation (in the presence of the cork substrates).

4.2. Structural Characterization and Photocatalytic Performance of the TiO₂ Functionalized Cork Substrates

4.2.1. X-ray Diffraction

XRD analyses were also carried out for the pristine cork substrate and for the TiO₂ functionalized cork substrate (Figure 7). It can be observed that the pristine cork substrate shows a broad peak centered at around $2\theta = 21^\circ$, indicating its amorphous nature [88,89]. When it comes to the functionalized cork substrate, five weak and broad peaks were detected, which can be associated with the presence of anatase. The XRD peaks observed at 25.3, 37.8, 48.0, 53.8, and 54.9° correspond to the (101), (004), (200), (105) and (211) reflections of the TiO₂ anatase phase. The results corroborate the XRD data obtained for the TiO₂ nanopowder (Figure 2), confirming the presence of TiO₂ anatase nanostructures at the surface of the cork.

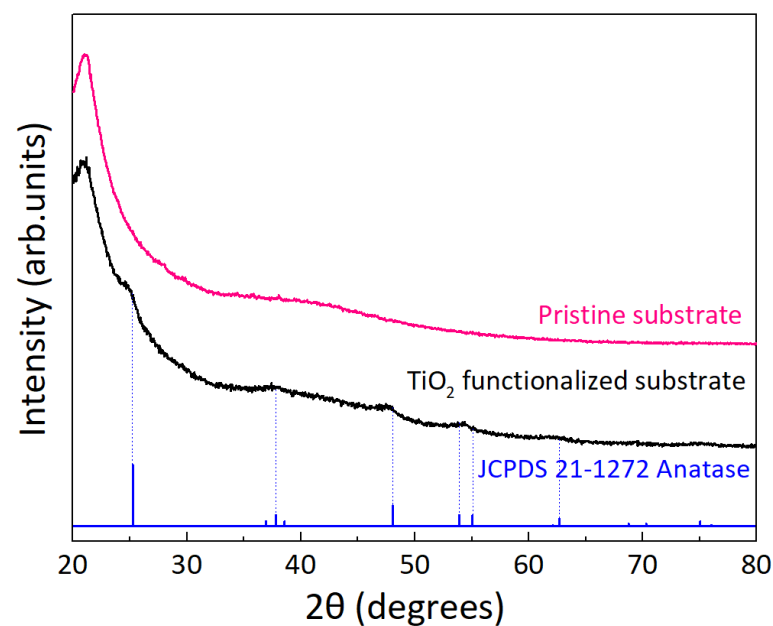


Figure 7. XRD diffractograms of the pristine and TiO₂ functionalized cork substrates. For comparison, the simulated TiO₂ anatase is presented.

4.2.2. Scanning Electron Microscopy

SEM images of the pristine cork substrates together with the functionalized ones are shown in Figure 8. In Figure 8a–c, the pristine cork is shown, which displays several closed and air-hollow unit cells, forming polygons in a regular honeycomb arrangement and the number of sides in these polygons varies. As reported for *Quercus suber* L., hexagonal, pentagonal and heptagonal cells are the most frequent, representing around 95% of the total forms [90]. The diameter of the cork cells is around 15–20 μm (see Figure 8a) and their size depends on the season in which they are formed [90]. For instance, early cork cells (cells formed in the main growth period) are greater in height and have thinner cell walls, while late cork cells (cells formed at the end of the growth period) are smaller and have a thicker wall [91,92]. In the specific case of *Quercus suber* L., for early cork cells, prism height ranges from 30–40 μm , prism base edges from 13–15 μm , average base area from $4\text{--}6 \times 10^{-6} \text{ cm}^2$ and the cell wall thickness between 1 and 1.5 μm . Late cork cells have a reduced prism height, nearly 10 μm , and the cell wall thickness almost doubles. The number of cells per cm^3 fluctuates from 4 to 7×10^7 for early cork and late cork from 10 to 20×10^7 [90]. Another important characteristic is the non-uniform undulations of the cell walls, which vary from cell to cell, as well as the roughness of their surface [93]. Some totally corrugated cells are observed, together with a few collapsed cells (see Figure 8a). Concerning the irregularities on the surface of the cells, granulates and small deposits are visible with no defined shape (Figure 8c) [91]. It is also visible that the interior of these cork cells is closed, without internal porosity.

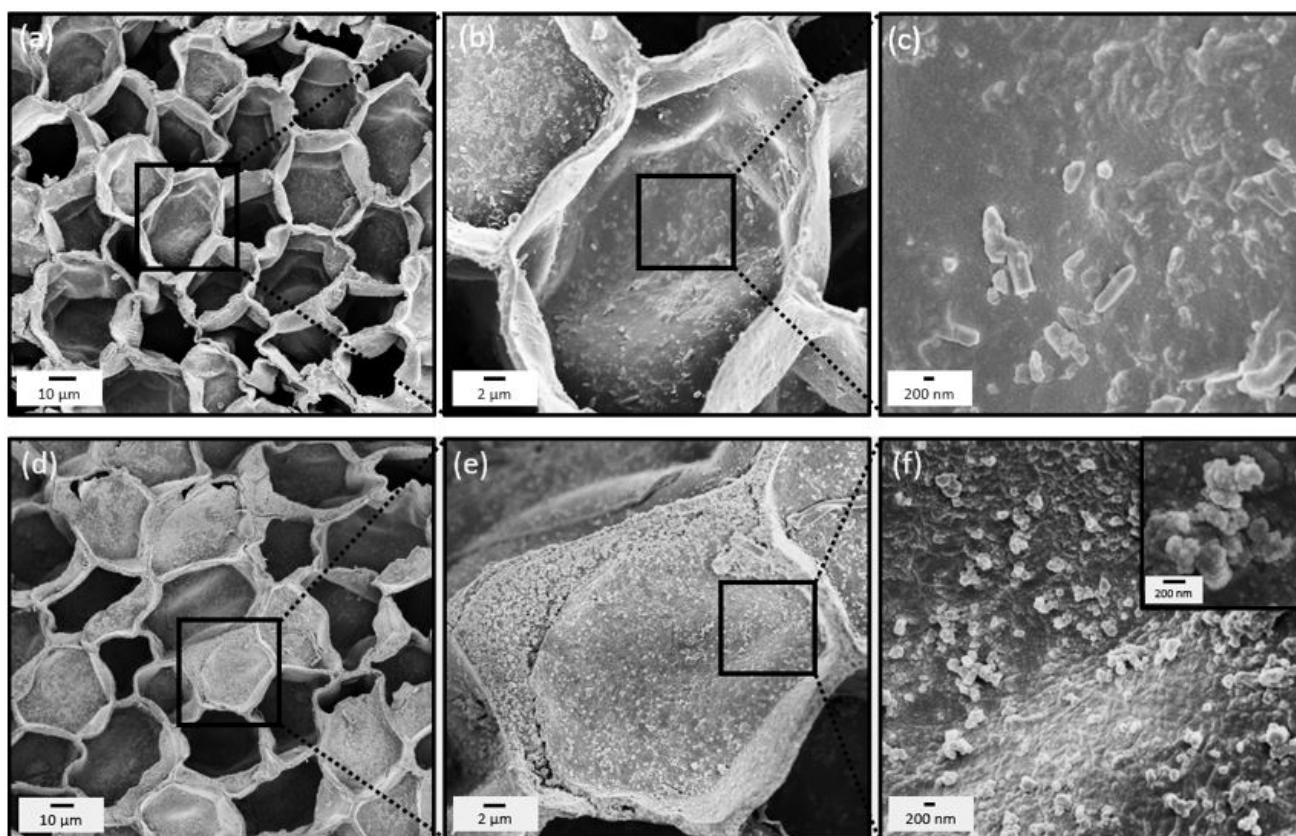


Figure 8. SEM images of the pristine cork substrates (a–c) together with the TiO_2 functionalized ones (d–f). The inset in (f) shows a TiO_2 nanoparticles' agglomerate at the interior of a cork's cell.

After the microwave synthesis (Figure 8d–f), it is possible to observe that the honeycomb arrangement of the cork cells is preserved. Additionally, the TiO_2 agglomerates of nanoparticles are clearly discernible at the surface of the cork, completely filling the cork cells and covering the substrate entirely, Figure 8f.

The chemical composition of the substrates before (pristine cork) and after the microwave synthesis (TiO₂ functionalized cork substrates) was analyzed by EDS (Figure S3). Figure S3a shows that the pristine cork substrates (C₁₂₃H₁₈₂O₅₆N for *Quercus suber* L. [94]) are mainly composed of C (Figure S3b) and O (Figure S3c), consistent with its chemical composition [88]. For the TiO₂ functionalized cork substrates, a uniform distribution of Ti (Figure S3g), together with C and O (Figure S3e,f) are observed. This indicates the homogeneous distribution of all elements on the surface of the cork.

4.3. Photocatalytic Activity of the TiO₂ Functionalized Cork Substrates

4.3.1. RhB Photocatalytic Degradation under Solar Simulating Light

The RhB decolorization in the presence of the cork substrates (pristine and functionalized with TiO₂) was evaluated under solar simulating light up to a total of 12 h. The aliquots of the dye were taken after 1 h (up to 4 h) and, after that time, every 2 h by using the UV-VIS spectrophotometer. A gradual decrease in the absorption peak of RhB (at 554 nm [95,96]) was observed over time. The decolorization rate (%) of the RhB dye was calculated accordingly to Equation (3):

$$\text{Decolorization (\%)} = \frac{A_0 - A_t}{A_0} \times 100 \quad (3)$$

where A_0 is the initial absorbance of the RhB solution before irradiation and A_t is the absorbance of RhB solution after a certain exposure time (t) [23,97]. Blank experiments (only RhB solution) were also carried out under solar simulating light and natural sunlight (Figures 9c and 10c). Although a slight increase in the RhB concentration is observed for both cases, possibly due to the evaporation of the solvent over time [68], no degradation of the RhB dye was observed in both cases, as reported in other studies [18,98].

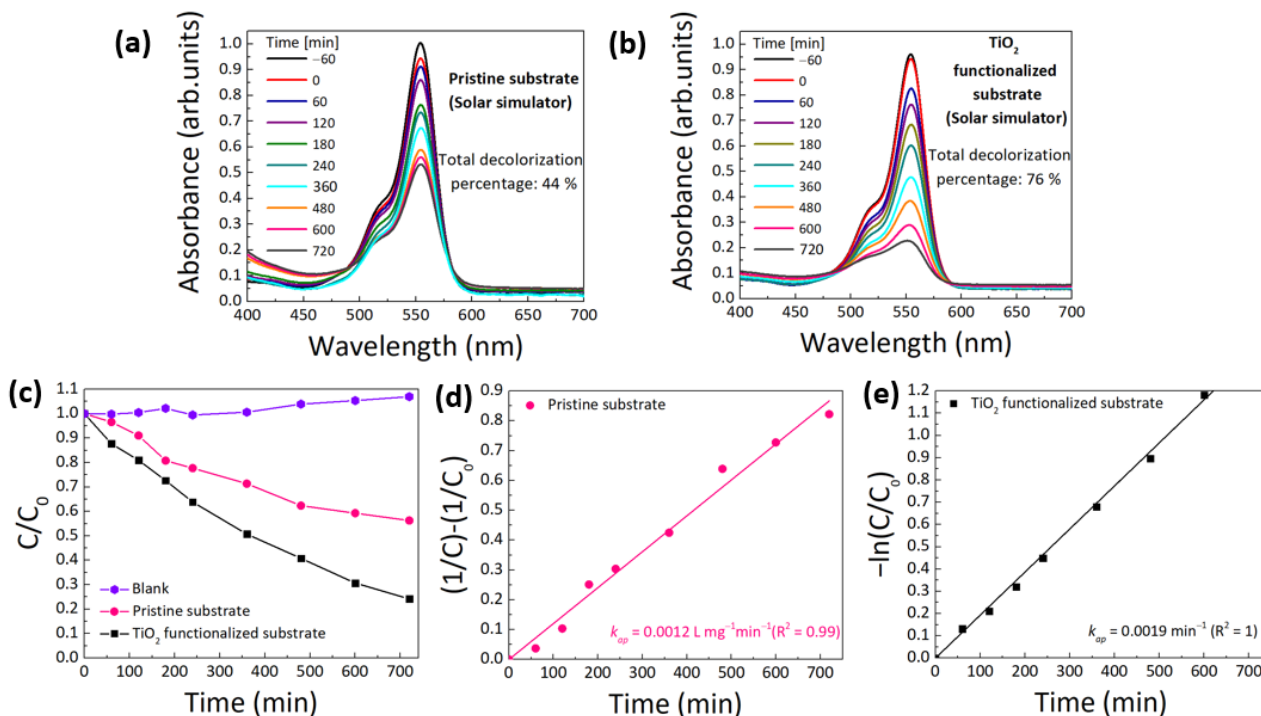


Figure 9. RhB absorbance spectra under simulated solar light radiation (LED simulator with AM 1.5 Spectrum) up to 12 h (720 min) for cork substrates: (a) pristine substrate and (b) TiO₂ functionalized substrate. (c) Decolorization ratio (C/C_0) of RhB dye without any substrate (blank), with the pristine and TiO₂ functionalized cork substrates, (d) pseudo-second-order kinetics for RhB decolorization in the presence of the pristine substrate and (e) pseudo-first-order kinetics for RhB decolorization in the presence of the TiO₂ functionalized substrate.

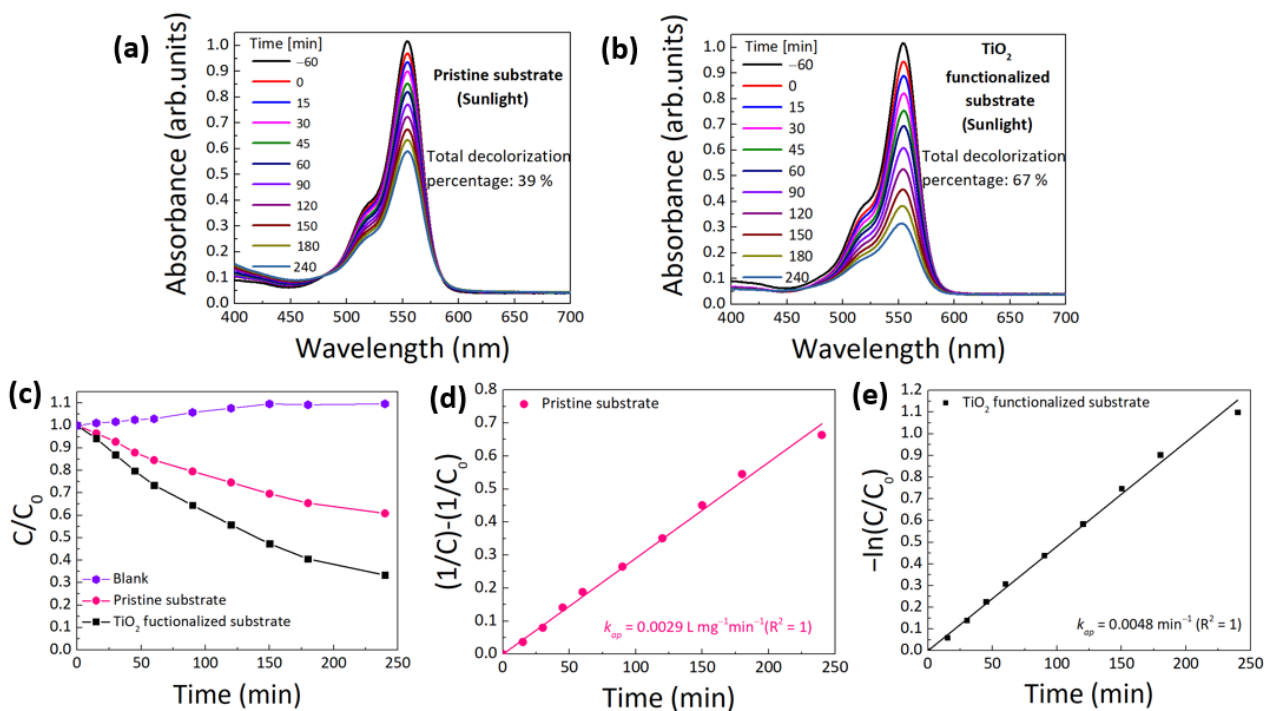


Figure 10. RhB absorbance spectra under natural sunlight up to 4 h (240 min) for cork substrates: (a) pristine substrate and (b) TiO₂ functionalized substrate. (c) Decolorization ratio (C/C_0) of RhB dye without any substrate (blank), with the pristine and TiO₂ functionalized cork substrates, (d) pseudo-second-order kinetics for RhB decolorization in the presence of the pristine substrate and (e) pseudo-first-order kinetics for RhB decolorization in the presence of the TiO₂ functionalized substrate.

Figure 9a shows a RhB decolorization of 44% without any catalyst on the surface of the cork after 12 h. The uptake of RhB molecules by the pristine cork stems from its honeycomb structure and cork cells' surface roughness, increasing the RhB adsorption capacity during the first few hours. However, after 8 h of light exposure, a tendency for stabilization is visible (Figure 9c). After that time, fewer trap sites on the cork surface could be available, leading to a decrease in the absorption rate. According to the literature, the adsorption kinetics model of organic pollutants on cork presents a convex initial curvature, indicating that the adsorption rate decreases with time: it becomes more difficult for the adsorbate to find free sites to adsorb since the main sites are being occupied [99]. This overall significant adsorption of RhB molecules by the pristine cork, which is visible with and without irradiation in Figure 9a, has also been previously reported [100].

It is also well established that suberin, the main chemical component of cork, is hydrophobic due to the existence of aliphatic substances bound to the aromatic domain as triacylglycerol esters. Lignin, the second most abundant chemical component of cork, is characterized by the presence of aromatic alcohol monolignols and acids (in particular, cinnamic and ferulic acid) [59,101,102]. It is reported that the aromatic domain of both suberin and lignin will determine the interaction between cork and the organic compounds, such as RhB [103], which are essentially hydrophobic [59,104]. As a result, these hydrophobic regions in cork will confer its special affinity to organic pollutants, and, hence, it is expected that an increase in the diffusion of hydrophobic dye molecules into cork will occur [104,105].

Meanwhile, with the TiO₂ functionalized cork substrate (Figure 9b), the decolorization efficiency was substantially increased to 76% for the same exposure time. This indicates that the synthesized TiO₂ nanomaterials effectively contributed to the degradation of RhB.

It is well known that different factors may influence the photocatalytic activity of TiO₂, such as the phase structure, crystallite size, specific surface area and exposed crystal facets [106,107]. As confirmed by TEM and SEM, particles in the nanometer range were

formed with an average size of ~5 nm. Smaller nanoparticles possess high specific surface area and surface-to-volume ratio [108]. As a consequence, more active sites on the catalyst are available to interact with the pollutant molecules [68]. Moreover, if the particle size is decreased, the distance that photogenerated electron-hole pairs need to travel is reduced, thus reducing the probability of recombination of photogenerated charge carriers [109]. It was also observed by TEM and SEM that these particles formed agglomerates. Such agglomerates influence the specific surface area of the nanoparticles and, consequently, their photocatalytic activity [23,110,111]. Several approaches and synthesis parameters can be used to minimize their formation including pH of the solution, addition of surfactants, among others. Nevertheless, the synthesized TiO₂ nanoparticles enhanced the cork's performance on the removal of RhB molecules from water (Figure 9a,b).

The (101) anatase surface is found to dominate the structure of nanosized anatase crystallites due to its energetic preference and higher stability, being labeled as the majority surface [112]. As observed in Figure 5, (101) anatase near-spherical nanocrystals without a specific facet on the crystal surface are largely present in the nanopowder produced. So, it has not been considered any RhB degradation contribution from active anatase facets.

Moreover, in general, it is accepted that for pure TiO₂ phases, anatase exhibits superior photocatalytic activity than the other two crystalline phases: rutile and brookite. Rutile and brookite are direct band gap semiconductors, while anatase presents an indirect band gap. Therefore, anatase TiO₂ has a longer lifetime of photogenerated electrons and holes. Additionally, the average effective mass of photogenerated electrons is the lightest compared to rutile and brookite, and, as a result, it exhibits the fastest migration of photogenerated electrons and holes from the interior to the surface of anatase particles. Hence, a lower recombination rate is expected with pure TiO₂ anatase, thus showing a better photocatalytic performance [106,113].

The RhB decolorization process in the presence of cork substrates was investigated by using the Langmuir–Hinshelwood model (Equation (4)):

$$r = -\frac{dC}{dt} = \frac{k_r K_{ad} C}{1 + K_{ad} C} \quad (4)$$

in which r represents the degradation rate, C the concentration of the organic pollutant, and K_{ad} the adsorption equilibrium constant. After integration in the interval $[C, C_0]$, it is simplified to the pseudo-first-order-kinetics equation with an apparent rate constant ($k_{ap} = k_r K_{ad}$), and if we consider that the adsorption is weak, as well as the concentration of organic pollutants, the factor $K_{ad}C$ can be negligible and, thus, Equation (5) is obtained [110]:

$$\ln\left(\frac{C}{C_0}\right) = -k_{ap}t \quad (5)$$

where k_{ap} is the photodegradation apparent rate constant, t is the time, C_0 is the initial concentration and C is the concentration at a certain time [23,114].

Based on Equation (5), the rate constants k_{ap} (min^{-1}) can be determined by plotting $-\ln\left(\frac{C}{C_0}\right)$ versus time [115], where the slope of the linear regressions are the apparent rate constants [23].

The obtained photodegradation apparent rate constant was found to be 0.0019 min^{-1} with TiO₂ functionalized substrate (Figure 9e), and it can be concluded that the photocatalytic dye degradation follows the pseudo-first-order kinetics, since a good correlation for the fitted line was obtained (R^2 above 0.95 [116]). In contrast with the TiO₂ functionalized substrate, the pristine cork substrate (Figure 9d) did not show satisfactory fitting for the pseudo-first-order equation (which has also already been reported [100]), but fitted well ($R^2 = 0.99$) the pseudo-second-order equation, described with the following equation:

$$\frac{1}{C} - \frac{1}{C_0} = k_{ap}t \quad (6)$$

Based on Equation (6), the rate constant can be obtained by a linear fit through the plot of $\frac{1}{C} - \frac{1}{C_0}$ versus time [117] and a value of $0.0012 \text{ L mg}^{-1} \text{ min}^{-1}$ was obtained. As mentioned before, this trend can be explained by a fast adsorption of RhB molecules in the first 8 h (480 min), followed by a slower uptake and a subsequent stabilization, since fewer adsorption sites are available.

4.3.2. RhB Photocatalytic Degradation under Natural Sunlight

RhB decolorization under natural sunlight was also monitored with the cork substrates (pristine and functionalized with TiO_2) within 4 h (240 min) (Figure 10). For comparison, the degree of RhB decolorization under solar simulating light up to 4 h, in the presence of both cork substrates, was also calculated and is summarized in Table 1. As indicated before, no stirring nor oxygenation were needed during the reactions. Figure S4 shows the floating characteristic of cork during the photocatalytic experiments under natural sunlight. The substrates can thus be easily collected from the solution.

Table 1. RhB decolorization percentages under solar simulating light and natural sunlight exposure up to 4 h.

| | | RhB Decolorization (%) |
|---------------------------|---|------------------------|
| Solar simulating light | Pristine substrate | 22 |
| | TiO_2 functionalized substrate | 36 |
| Natural sunlight exposure | Pristine substrate | 39 |
| | TiO_2 functionalized substrate | 67 |

Table 1 shows that in the presence of the pristine substrate, a difference in the RhB decolorization is observed: 22% versus 39% of degradation under solar simulating light and natural sunlight, respectively. Cork's chemical components may degrade upon prolonged UV light irradiation [118]. In fact, the absorption of UV light by pristine cork under natural sunlight might lead to the photooxidation of cellulose, hemicellulose, and degradation of some lignin content present in cork, which could generate chromophore groups, such as carboxylic acids, quinones and hydroperoxide radicals. As a result, these chromophore groups could trigger photochemical reactions on the cork surface, thus promoting a faster decolorization of RhB, in comparison with solar simulating light exposure [119–121]. For the TiO_2 functionalized cork substrates, as observed, an increase in decolorization efficiency by 31% was obtained under natural sunlight when compared to solar simulating for 4 h. In contrast with the solar spectrum, which is composed of around 5% UV light, 43% visible light and 50% IR light [122], the LED solar simulator used in the photocatalytic experiments mainly provides visible light (the irradiance is cut for shorter wavelengths (high UV energy)), as observed in Figure S5. Since TiO_2 anatase has a wide band gap value ($\sim 3.2 \text{ eV}$), it is mostly photoactive in the UV region [123], and so the difference may be due to the UV light contribution of natural sunlight. This is also supported by the obtained apparent rate constants with the TiO_2 functionalized substrate under natural sunlight, as visible in Figure 10 and under solar simulating light (Figure 9e). The reaction was 2.5 times faster under natural sunlight ($k_{\text{ap}} = 0.0048 \text{ min}^{-1}$) than under the solar simulating light (0.0019 min^{-1}) in a third of the time (12 h under solar simulating light compared to 4 h under natural sunlight).

4.3.3. Reusability Tests under Natural Sunlight

Reusability tests are of great importance to evaluate the stability of the photocatalyst [124]. Since the best results were obtained under natural sunlight, reusability tests with the TiO_2 functionalized cork substrate were performed under three consecutive cycles within 4 h (240 min) under natural sunlight. Figure 11 shows the decolorization ratio (C/C_0) of the RhB dye, the pseudo-first-order model fitting for RhB decolorization under three cycles and a column chart of RhB decolorization efficiency with the number of uses. A summary of the obtained results is also presented in Table 2.

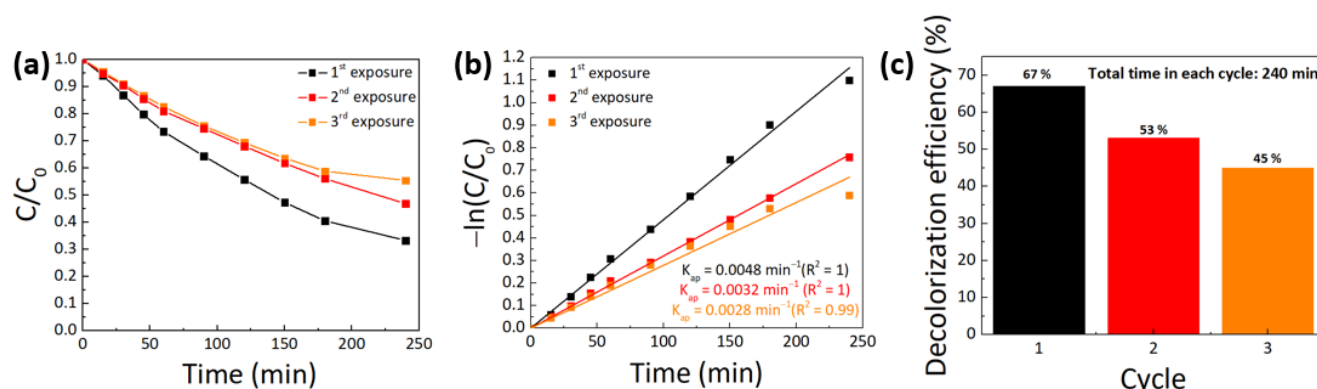


Figure 11. Reusability tests under natural sunlight over 3 degradation cycles with the TiO₂ functionalized cork substrate: (a) decolorization ratio (C/C_0) of the RhB dye, (b) pseudo-first-order kinetics for the RhB decolorization and (c) decolorization efficiency (%) versus the number of cycles.

Table 2. Kinetic parameters (rate constants k_{ap} and linear regression coefficients R^2) for the RhB decolorization under natural sunlight (1st, 2nd and 3rd exposures) up to 4 h with the TiO₂ functionalized cork substrate.

| | | k_{ap} (min ⁻¹) | R^2 |
|-------------------|--------------------------------------|-------------------------------|-------|
| 1st sunlight exp. | Pseudo-first-order kinetics reaction | 0.005 | 1 |
| 2nd sunlight exp. | | 0.003 | 1 |
| 3rd sunlight exp. | | 0.003 | 0.99 |

In Table 2 and Figure 11, a decrease in photocatalytic activity was observed with the number of exposures. The reaction rate decreased from 0.005 min^{-1} in the first cycle to 0.003 min^{-1} in the third cycle. After performing three consecutive cycles, a decolorization efficiency loss of around 22% was obtained. Since neither heat/UV treatments nor rinsing were applied to the substrate between cycles, a high percentage of RhB molecules could have remained from the previous cycle adsorbed on the photocatalyst surface, hindering the available pore sites on the TiO₂ functionalized cork substrate for reaction [13,125], thus decreasing its overall cycling efficiency. This effect has been previously reported in different studies [13,23,125,126].

It is worth mentioning that this work demonstrates the real contribution of the RhB molecules' adsorption on pristine cork substrates, with a direct effect on the overall photocatalytic activity of the floating photocatalysts.

5. Conclusions

TiO₂ nanomaterials were directly synthesized on cork substrates by a fast and low temperature solvothermal method under microwave irradiation (120 °C for 1 h), without any preliminary process by using oxalic acid. These nanomaterials were characterized in powder form, as well as functionalized on cork substrates. The characterization of TiO₂ nanopowder by XRD, Raman spectroscopy and TEM revealed the presence of the TiO₂ anatase structure. Although some FTIR bands indicated the presence of cork's organic species on TiO₂ nanopowder, crystalline TiO₂ anatase nanoparticles were formed on cork, as proved by XRD data. The obtained brown powdered TiO₂ material showed a broad absorption band peaked at ~306 nm, which extended through the visible range up to 800 nm. SEM and EDS analyses of the TiO₂ functionalized substrates showed the formation of nearly spherical TiO₂ nanoparticles that uniformly covered the honeycomb cells of cork. The best RhB decolorization efficiency was obtained with the TiO₂ functionalized cork substrate under natural sunlight, and a RhB degradation of 67% was obtained compared to 39% with the pristine cork substrate, in 4 h of natural light exposure. In the presence of the TiO₂ functionalized substrates, the photocatalytic reaction was 2.5 times faster under natural sunlight than under solar simulating light, in a third of the time (12 h under

solar simulating light compared to 4 h under natural sunlight). In summary, the results presented show that by using a simple microwave approach, cork floating catalysts based on TiO₂-materials can be employed for removing organic pollutants from water under natural sunlight.

Supplementary Materials: The following supporting information can be downloaded at: <https://www.mdpi.com/article/10.3390/su14159645/s1>, Figure S1: Raman spectra of the cork substrates (pristine and TiO₂ functionalized one). Figure S2: Absorption curve of the synthesized TiO₂ nanopowder (in the absence of the cork substrates). The inset shows the SEM image of the TiO₂ nanopowder. Figure S3: SEM images of the cork substrates: (a) pristine substrate and (d) TiO₂ functionalized substrate. The corresponding EDS maps of C ((b) and (e)), O ((c) and (f)) and Ti (g) are also visible. Figure S4: Photocatalytic experiments with the cork substrates under natural sunlight: (a) pristine substrate and (b) TiO₂ functionalized substrate. Figure S5: Spectral irradiance versus wavelength (from 400 to 1100 nm) of the MiniSol model LSH-7320 and the reference AM 1.5.

Author Contributions: M.L.M. was responsible for producing and characterizing the materials, as well as writing the manuscript. M.M. and F.X.V. were responsible for the photocatalytic experiments. A.P. and D.N. were responsible for the overall scientific orientation and revising the manuscript. D.N. was also responsible for the TEM measurements. A.S.R.M. and J.R. participated in the review and editing. E.F. and R.M. were responsible for supervising all the process and getting funding. All authors have read and agreed to the published version of the manuscript.

Funding: This work was financed by national funds from FCT—Fundação para a Ciência e a Tecnologia, I.P., in the scope of the projects LA/P/0037/2020, UIDP/50025/2020, and UIDB/50025/2020 of the Associate Laboratory Institute of Nanostructures, Nanomodelling, and Nanofabrication—i3N, but also the UI/BD/151292/2021 (Ph.D. research scholarship). The work was also partially funded by the Nanomark collaborative project between INCM (Imprensa Nacional—Casa da Moeda) and CENIMAT/i3N. Acknowledgments also go to the EC project SYNERGY H2020-WIDESPREAD-2020-5, CSA, proposal n° 952169, EMERGE-2020-INFRAIA-2020-1, proposal n° 101008701, and to the European Community's H2020 program under grant agreement No. 787410 (ERC-2018-AdG DIGISMART).

Institutional Review Board Statement: Not applicable.

Informed Consent Statement: Not applicable.

Data Availability Statement: Not applicable.

Conflicts of Interest: The authors declare no conflict of interest.

References

1. Nan Chong, M.; Jin, B.; Chow, C.W.; Saint, C. Recent developments in photocatalytic water treatment technology: A review. *Water Res.* **2010**, *44*, 2997–3027. [[CrossRef](#)] [[PubMed](#)]
2. Fernandes, E.M.; Pires, R.A.; Reis, R.L. 17—Cork biomass biocomposites: Lightweight and sustainable materials. In *Lignocellulosic Fibre and Biomass-Based Composite Materials: Processing, Properties and Applications*; Woodhead Publishing: Sawston, UK, 2017; pp. 365–385. ISBN 9780081009666.
3. Su, K.; Li, L.; Deng, S.; Gao, Z.; Qin, Q.; Yang, J.; Zhang, S.; Chen, J. Research progress of TiO₂ photocatalytic reduction of oxyanion pollutants in water: A mini review. *Green Chem. Lett. Rev.* **2021**, *15*, 35–44. [[CrossRef](#)]
4. Ren, G.; Han, H.; Wang, Y.; Liu, S.; Zhao, J.; Meng, X.; Li, Z. Recent Advances of Photocatalytic Application in Water Treatment: A Review. *Nanomaterials* **2021**, *11*, 1804. [[CrossRef](#)] [[PubMed](#)]
5. Liu, Q. Pollution and Treatment of Dye Waste-Water. *IOP Conf. Ser. Earth Environ. Sci.* **2020**, *514*, 052001. [[CrossRef](#)]
6. Al-Tohamy, R.; Ali, S.S.; Li, F.; Okasha, K.M.; Mahmoud, Y.A.G.; Elsamahy, T.; Jiao, H.; Fu, Y.; Sun, J. A critical review on the treatment of dye-containing wastewater: Ecotoxicological and health concerns of textile dyes and possible remediation approaches for environmental safety. *Ecotoxicol. Environ. Saf.* **2022**, *231*, 113160. [[CrossRef](#)] [[PubMed](#)]
7. Ismail, W.N.W.; Mokhtar, S.U. Various Methods for Removal, Treatment, and Detection of Emerging Water Contaminants. In *Emerging Contaminants*; IntechOpen: London, UK, 2020.
8. Mamba, F.B.; Mbuli, B.S.; Ramontja, J. Recent Advances in Biopolymeric Membranes towards the Removal of Emerging Organic Pollutants from Water. *Membranes* **2021**, *11*, 798. [[CrossRef](#)] [[PubMed](#)]
9. Singh, N.; Goldsmith, B.R. Role of Electrocatalysis in the Remediation of Water Pollutants. *ACS Catal.* **2020**, *10*, 3365–3371. [[CrossRef](#)]
10. Hu, X.; Yip, A.C.K. Heterogeneous Catalysis: Enabling a Sustainable Future. *Front. Catal.* **2021**, *1*, 667675. [[CrossRef](#)]

11. Schneider, J.; Matsuoka, M.; Takeuchi, M.; Zhang, J.; Horiuchi, Y.; Anpo, M.; Bahnemann, D.W. Understanding TiO₂ Photocatalysis: Mechanisms and Materials. *Chem. Rev.* **2014**, *114*, 9919–9986. [[CrossRef](#)]
12. Rani, S.; Aggarwal, M.; Kumar, M.; Sharma, S.; Kumar, D. Removal of methylene blue and rhodamine B from water by zirconium oxide/graphene. *Water Sci.* **2016**, *30*, 51–60. [[CrossRef](#)]
13. Nunes, D.; Fragoso, A.R.; Freire, T.; Matias, M.; Marques, A.C.; Martins, R.; Fortunato, E.; Pimentel, A. Ultrafast Microwave Synthesis of WO₃ Nanostructured Films for Solar Photocatalysis. *Phys. Status Solidi RRL Rapid Res. Lett.* **2021**, *15*, 2100196. [[CrossRef](#)]
14. Sharma, M.; Murugavel, S.; Dinesh, S.; De Groot, F.M.F. Reversal in the Lattice Contraction of α -Fe₂O₃ Nanoparticles. *J. Phys. Chem. C* **2018**, *122*, 9292–9301. [[CrossRef](#)]
15. Reddy, C.V.; Babu, B.; Reddy, I.N.; Shim, J. Synthesis and characterization of pure tetragonal ZrO₂ nanoparticles with enhanced photocatalytic activity. *Ceram. Int.* **2018**, *44*, 6940–6948. [[CrossRef](#)]
16. Jiang, J.; Kato, K.; Fujimori, H.; Yamakata, A.; Sakata, Y. Investigation on the highly active SrTiO₃ photocatalyst toward overall H₂O splitting by doping Na ion. *J. Catal.* **2020**, *390*, 81–89. [[CrossRef](#)]
17. Pimentel, A.; Rodrigues, J.; Duarte, P.; Nunes, D.; Costa, F.M.; Monteiro, T.; Martins, R.; Fortunato, E. Effect of solvents on ZnO nanostructures synthesized by solvothermal method assisted by microwave radiation: A photocatalytic study. *J. Mater. Sci.* **2015**, *50*, 5777–5787. [[CrossRef](#)]
18. Ferreira, S.H.; Morais, M.; Nunes, D.; Oliveira, M.J.; Rovisco, A.; Pimentel, A.; Águas, H.; Fortunato, E.; Martins, R. High UV and Sunlight Photocatalytic Performance of Porous ZnO Nanostructures Synthesized by a Facile and Fast Microwave Hydrothermal Method. *Materials* **2021**, *14*, 2385. [[CrossRef](#)]
19. Pawar, M.; Sendogdular, S.T.; Gouma, P. A brief overview of TiO₂ photocatalyst for organic dye remediation: Case study of reaction mechanisms involved in Ce-TiO₂ photocatalysts system. *J. Nanomater.* **2018**, *2018*, 5953609. [[CrossRef](#)]
20. Nunes, D.; Pimentel, A.; Araujo, A.; Calmeiro, T.R.; Panigrahi, S.; Pinto, J.V.; Barquinha, P.; Gama, M.; Fortunato, E.; Martins, R. Enhanced UV Flexible Photodetectors and Photocatalysts Based on TiO₂ Nanoplatforms. *Top. Catal.* **2018**, *61*, 1591–1606. [[CrossRef](#)]
21. Pimentel, A.; Nunes, D.; Pereira, S.; Martins, R.; Fortunato, E. Photocatalytic Activity of TiO₂ Nanostructured Arrays Prepared by Microwave-Assisted Solvothermal Method. In *Semiconductor Photocatalysis—Materials, Mechanisms and Applications*; IntechOpen: London, UK, 2016; Chapter 3.
22. Landolsi, Z.; Ben Assaker, I.; Nunes, D.; Fortunato, E.; Martins, R.; Chtourou, R.; Ammar, S. Enhanced electrical and photocatalytic properties of porous TiO₂ thin films decorated with Fe₂O₃ nanoparticles. *J. Mater. Sci. Mater. Electron.* **2020**, *31*, 20753–20773. [[CrossRef](#)]
23. Matias, M.L.; Pimentel, A.; Reis-Machado, A.S.; Rodrigues, J.; Deuermeier, J.; Fortunato, E.; Martins, R.; Nunes, D. Enhanced Fe-TiO₂ Solar Photocatalysts on Porous Platforms for Water Purification. *Nanomaterials* **2022**, *12*, 1005. [[CrossRef](#)]
24. Nunes, D.; Pimentel, A.; Pinto, J.V.; Calmeiro, T.R.; Nandy, S.; Barquinha, P.; Pereira, L.; Carvalho, P.A.; Fortunato, E.; Martins, R. Photocatalytic behavior of TiO₂ films synthesized by microwave irradiation. *Catal. Today* **2016**, *278*, 262–270. [[CrossRef](#)]
25. Hashimoto, K.; Irie, H.; Fujishima, A. TiO₂ Photocatalysis: A Historical Overview and Future Prospects. *Jpn. J. Appl. Phys.* **2005**, *44*, 8269–8285. [[CrossRef](#)]
26. He, F.; Jeon, W.; Choi, W. Photocatalytic air purification mimicking the self-cleaning process of the atmosphere. *Nat. Commun.* **2021**, *12*, 2528. [[CrossRef](#)] [[PubMed](#)]
27. Fernández-Catalá, J.; Berenguer-Murcia, Á.; Cazorla-Amorós, D. Photocatalytic oxidation of VOCs in gas phase using capillary microreactors with commercial TiO₂ (P25) fillings. *Materials* **2018**, *11*, 1149. [[CrossRef](#)]
28. Nunes, D.; Pimentel, A.; Branquinho, R.; Fortunato, E.; Martins, R. Metal oxide-based photocatalytic paper: A green alternative for environmental remediation. *Catalysts* **2021**, *11*, 504. [[CrossRef](#)]
29. Nakata, K.; Fujishima, A. TiO₂ photocatalysis: Design and applications. *J. Photochem. Photobiol. C Photochem. Rev.* **2012**, *13*, 169–189. [[CrossRef](#)]
30. Xu, H.; Ouyang, S.; Liu, L.; Reunchan, P.; Umezawa, N.; Ye, J. Recent advances in TiO₂-based photocatalysis. *J. Mater. Chem. A* **2014**, *2*, 12642–12661. [[CrossRef](#)]
31. Heng, Z.W.; Chong, W.C.; Pang, Y.L.; Sim, L.C.; Koo, C.H. Photocatalytic degradation of organic pollutants using green oil palm frond-derived carbon quantum dots/titanium dioxide as multifunctional photocatalysts under visible light radiation. *Chin. J. Chem. Eng.* **2021**, *12*, 1–31. [[CrossRef](#)]
32. Reda, S.M.; Khairy, M.; Mousa, M.A. Photocatalytic activity of nitrogen and copper doped TiO₂ nanoparticles prepared by microwave-assisted sol-gel process. *Arab. J. Chem.* **2020**, *13*, 86–95. [[CrossRef](#)]
33. Humayun, M.; Raziq, F.; Khan, A.; Luo, W. Modification strategies of TiO₂ for potential applications in photocatalysis: A critical review. *Green Chem. Lett. Rev.* **2018**, *11*, 86–102. [[CrossRef](#)]
34. Zhao, J.; Chen, C.; Ma, W. Photocatalytic Degradation of Organic Pollutants Under Visible Light Irradiation. *Top. Catal.* **2005**, *35*, 269–278. [[CrossRef](#)]
35. Gusain, R.; Kumar, N.; Ray, S.S. Chapter 8—Factors Influencing the Photocatalytic Activity of Photocatalysts in Wastewater Treatment. In *Photocatalysts in Advanced Oxidation Processes for Wastewater Treatment*; Fosso-Kankeu, E., Pandey, S., Sinha Ray, S., Eds.; John Wiley & Sons Ltd.: Hoboken, NJ, USA, 2020; pp. 229–270.
36. Xu, N.; Shi, Z.; Fan, Y.; Dong, J.; Shi, J.; Hu, M.Z.C. Effects of Particle Size of TiO₂ on Photocatalytic Degradation of Methylene Blue in Aqueous Suspensions. *Ind. Eng. Chem. Res.* **1999**, *38*, 373–379. [[CrossRef](#)]

37. Danish, M.S.S.; Estrella, L.L.; Alemaida, I.M.A.; Lisin, A.; Moiseev, N.; Ahmadi, M.; Nazari, M.; Wali, M.; Zaheb, H.; Senjyu, T.; et al. Photocatalytic Applications of Metal Oxides for Sustainable Environmental Remediation. *Metals* **2021**, *11*, 80. [[CrossRef](#)]
38. Bharati, B.; Sonkar, A.K.; Singh, N.; Dash, D.; Rath, C. Enhanced photocatalytic degradation of dyes under sunlight using biocompatible TiO₂ nanoparticles. *Mater. Res. Express* **2017**, *4*, 085503. [[CrossRef](#)]
39. Vishwanathan, S.; Laxmi, S.; Nandan, S.; Jayan, S.; Lijo, M.; Das, S. Effect of experimental parameters on photocatalytic degradation efficiency of TiO₂ nanoparticles synthesized by electrochemical method towards Rhodamine B dye solution under natural sunlight. *Environ. Sci. Pollut. Res.* **2022**, 1–16. [[CrossRef](#)]
40. Dubey, R.S.; Krishnamurthy, K.V.; Singh, S. Experimental studies of TiO₂ nanoparticles synthesized by sol-gel and solvothermal routes for DSSCs application. *Results Phys.* **2019**, *14*, 102390. [[CrossRef](#)]
41. Khairy, M.; Zakaria, W. Effect of metal-doping of TiO₂ nanoparticles on their photocatalytic activities toward removal of organic dyes. *Egypt. J. Pet.* **2014**, *23*, 419–426. [[CrossRef](#)]
42. Scuderi, V.; Impellizzeri, G.; Romano, L.; Scuderi, M.; Nicotra, G.; Bergum, K.; Irrera, A.; Svensson, B.G.; Privitera, V. TiO₂-coated nanostructures for dye photo-degradation in water. *Nanoscale Res. Lett.* **2014**, *9*, 458. [[CrossRef](#)]
43. Maragatha, J.; Rajendran, S.; Endo, T.; Karupuchamy, S. Microwave synthesis of metal doped TiO₂ for photocatalytic applications. *J. Mater. Sci. Mater. Electron.* **2017**, *28*, 5281–5287. [[CrossRef](#)]
44. Boyadzhiev, S.; Georgieva, V.; Rassovska, M. Characterization of reactive sputtered TiO₂ thin films for gas sensor applications. *J. Phys. Conf. Ser.* **2010**, *253*, 012040. [[CrossRef](#)]
45. Nunes, D.; Pimentel, A.; Santos, L.; Barquinha, P.; Fortunato, E.; Martins, R. Photocatalytic TiO₂ Nanorod Spheres and Arrays Compatible with Flexible Applications. *Catalysts* **2017**, *7*, 60. [[CrossRef](#)]
46. Senthil Kumar, R.; Gnanavel, B.; Jegatheesan, A. Microwave assisted synthesis and characterization of pure and Cr doped TiO₂ with improved photo-efficiency. *J. Mater. Sci. Mater. Electron.* **2018**, *29*, 6501–6510. [[CrossRef](#)]
47. Machut, C.; Kania, N.; Léger, B.; Wyrwalski, F.; Noël, S.; Addad, A.; Monflier, E.; Ponchel, A. Fast Microwave Synthesis of Gold-Doped TiO₂ Assisted by Modified Cyclodextrins for Photocatalytic Degradation of Dye and Hydrogen Production. *Catalysts* **2020**, *10*, 801. [[CrossRef](#)]
48. Vinodhini, J.; Mayandi, J.; Atchudan, R.; Jayabal, P.; Sasirekha, V.; Pearce, J. Effect of microwave power irradiation on TiO₂ nano-structures and binder free paste screen printed dye sensitized solar cells. *Ceram. Int.* **2019**, *45*, 4667–4673. [[CrossRef](#)]
49. Strapasson, G.B.; Scheffer, F.R.; Cendron, S.W.; Silva, F.D.C.; Lazzari, N.H.; Azambuja, C.; Peyrot, A.; Weibel, D.E. Visible light sensitization of TiO₂/Ag/N nanostructures synthesized by microwave irradiation for oxidative degradation of organic dyes. *SN Appl. Sci.* **2020**, *2*, 543. [[CrossRef](#)]
50. Sboui, M.; Nsib, M.F.; Rayes, A.; Swaminathan, M.; Houas, A. TiO₂-PANI/Cork composite: A new floating photocatalyst for the treatment of organic pollutants under sunlight irradiation. *J. Environ. Sci.* **2017**, *60*, 3–13. [[CrossRef](#)]
51. Machado, L.C.R.; Torchia, C.B.; Lago, R.M. Floating photocatalysts based on TiO₂ supported on high surface area exfoliated vermiculite for water decontamination. *Catal. Commun.* **2006**, *8*, 538–541. [[CrossRef](#)]
52. Pullar, R.C.; Accaries, A.; Scheffer, D.G.H.; Caetano, A.P.F.; Novais, R.M. Cork derived TiO₂ biomorphic ecoceramics. *Open Ceram.* **2022**, *9*, 100243. [[CrossRef](#)]
53. Silva, S.P.; Sabino, M.A.; Fernandes, E.M.; Correló, V.M.; Boesel, L.F.; Reis, R.L. Cork: Properties, capabilities and applications. *Int. Mater. Rev.* **2005**, *50*, 345–365. [[CrossRef](#)]
54. Alves, H.F. Cork as a Raw Material for Antibacterial Membranes and Fibers. Master's Thesis, FCT-UNL, Lisbon, Portugal, 2019.
55. Pasalodos-Tato, M.; Pukkala, T.; Cañellas, I.; Sánchez-González, M. Optimizing the debarking and cutting schedule of cork oak stands. *Ann. For. Sci.* **2018**, *75*, 61. [[CrossRef](#)]
56. Rei, R.B. Melhoria do Processo de Lavação de Rolhas de Cortiça. Master's Thesis, Universidade de Aveiro, Aveiro, Portugal, 2015.
57. Castro, M.; Nogueira, V.; Lopes, I.; Vieira, M.N.; Rocha-Santos, T.; Pereira, R. Treatment of a textile effluent by adsorption with cork granules and titanium dioxide nanomaterial. *J. Environ. Sci. Health Part A* **2018**, *53*, 524–536. [[CrossRef](#)] [[PubMed](#)]
58. Duarte Vieira, H. Análise de Características da Cortiça Amadia Relevantes para a sua Qualidade Industrial. Master's Thesis, Instituto Superior de Agronomia, Lisbon, Portugal, 2009.
59. Pirozzi, C.; Pontoni, L.; Fabbicino, M.; Bogush, A.; Campos, L.C. Effect of organic matter release from natural cork used on bisphenol a removal from aqueous solution. *J. Clean. Prod.* **2020**, *244*, 118675. [[CrossRef](#)]
60. Nandy, S.; Fortunato, E.; Martins, R. Green economy and waste management: An inevitable plan for materials science. *Prog. Nat. Sci. Mater. Int.* **2022**, *32*, 1–9. [[CrossRef](#)]
61. Mohamad Idris, N.H.; Rajakumar, J.; Cheong, K.Y.; Kennedy, B.J.; Ohno, T.; Yamakata, A.; Lee, H.L. Titanium Dioxide/Polyvinyl Alcohol/Cork Nanocomposite: A Floating Photocatalyst for the Degradation of Methylene Blue under Irradiation of a Visible Light Source. *ACS Omega* **2021**, *6*, 14493–14503. [[CrossRef](#)] [[PubMed](#)]
62. Martins, C.I.; Gil, V. Processing-Structure-Properties of Cork Polymer Composites. *Front. Mater.* **2020**, *7*, 297. [[CrossRef](#)]
63. Iwashita, N. X-ray Powder Diffraction. In *Materials Science and Engineering of Carbon: Characterization*; Inagaki, M., Kang, F., Eds.; Butterworth-Heinemann: Oxford, UK, 2016; pp. 7–25.
64. Degen, T.; Sadki, M.; Bron, E.; König, U.; Nénert, G. The HighScore suite. *Powder Diffr.* **2014**, *29*, S13–S18. [[CrossRef](#)]
65. Chettah, W.; Barama, S.; Medjram, M.S.; Selmane, M.; Montero, D.; Davidson, A.; Védrine, J.C. Anatase titania activated by Cu(II) or Zn(II) nanoparticles for the photooxidation of methanol assisted by Rhodamine-B. *Mater. Chem. Phys.* **2021**, *257*, 123714. [[CrossRef](#)]

66. Bokuniaeva, A.O.; Vorokh, A.S. Estimation of particle size using the Debye equation and the Scherrer formula for polyphasic TiO₂ powder. *J. Phys. Conf. Ser.* **2019**, *1410*, 012057. [CrossRef]
67. Instituto Português do Mar e da Atmosfera. Available online: <https://www.ipma.pt/pt/index.html> (accessed on 9 May 2022).
68. Freire, T.; Fragoso, A.R.; Matias, M.; Vaz Pinto, J.; Marques, A.C.; Pimentel, A.; Barquinha, P.; Huertas, R.; Fortunato, E.; Martins, R.; et al. Enhanced solar photocatalysis of TiO₂ nanoparticles and nanostructured thin films grown on paper. *Nano Express* **2021**, *2*, 040002. [CrossRef]
69. Ohsaka, T.; Fujiki, I.; Fujiki, Y. Raman Spectrum of Anatase, TiO₂. *J. Raman Spectrosc.* **1978**, *7*, 321–324. [CrossRef]
70. El-Deen, S.S.; Hashem, A.M.; Abdel Ghany, A.E.; Indris, S.; Ehrenberg, H.; Mauger, A.; Julien, C.M. Anatase TiO₂ nanoparticles for lithium-ion batteries. *Ionics* **2018**, *24*, 2925–2934. [CrossRef]
71. Shyniya, C.R.; Bhabu, K.A.; Rajasekaran, T.R. Enhanced electrochemical behavior of novel acceptor doped titanium dioxide catalysts for photocatalytic applications. *J. Mater. Sci. Mater. Electron.* **2017**, *28*, 6959–6970. [CrossRef]
72. Praveen, P.; Viruthagiri, G.; Mugundan, S.; Shanmugam, N. Structural, optical and morphological analyses of pristine titanium di-oxide nanoparticles—Synthesized via sol-gel route. *Spectrochim. Acta Part A Mol. Biomol. Spectrosc.* **2014**, *117*, 622–629. [CrossRef]
73. Chougala, L.S.; Yatnatti, M.S.; Linganagoudar, R.K.; Kamble, R.R.; Kadadevarmath, J.S. A simple approach on synthesis of TiO₂ nanoparticles and its application in dye sensitized solar cells. *J. Nano Electron. Phys.* **2017**, *9*, 1–6. [CrossRef]
74. Alsharaeh, E.H.; Bora, T.; Soliman, A.; Ahmed, F.; Bharath, G.; Ghoniem, M.G.; Abu-Salah, K.M.; Dutta, J. Sol-Gel-Assisted Microwave-Derived Synthesis of Anatase Ag/TiO₂/GO Nanohybrids toward Efficient Visible Light Phenol Degradation. *Catalysts* **2017**, *7*, 133. [CrossRef]
75. Tan, C.; Tirri, T.; Wilen, C.-E. Investigation on the Influence of Chain Extenders on the Performance of One-Component Moisture-Curable Polyurethane Adhesives. *Polymers* **2017**, *9*, 184. [CrossRef]
76. Dietz, J. 5 Functionalization and Characterization of Isocyanate Modified Lignins. In *Synthesis and Characterization of Novel Functional Lignins—Towards Bio-Based Polyurethane Materials*; Apprimus Wissenschaftsverlag: Aachen, Germany, 2015; Volume 1, p. 75. ISBN 3863593758.
77. Nishimura, H.; Kamiya, A.; Nagata, T.; Katahira, M.; Watanabe, T. Direct evidence for α ether linkage between lignin and carbohydrates in wood cell walls. *Sci. Rep.* **2018**, *8*, 6538. [CrossRef]
78. Novais, R.M.; Caetano, A.P.F.; Seabra, M.P.; Labrincha, J.A.; Pullar, R.C. Extremely fast and efficient methylene blue adsorption using eco-friendly cork and paper waste-based activated carbon adsorbents. *J. Clean. Prod.* **2018**, *197*, 1137–1147. [CrossRef]
79. Mislata, A.M.; Puxeu, M.; Ferrer-Gallego, R. Aromatic Potential and Bioactivity of Cork Stoppers and Cork By-Products. *Foods* **2020**, *9*, 133. [CrossRef]
80. Graça, J.; Santos, S. Glycerol-derived ester oligomers from cork suberin. *Chem. Phys. Lipids* **2006**, *144*, 96–107. [CrossRef]
81. Barros-Timmons, A.; Lopes, M.H.; Pascoal Neto, C.; Dhanabalan, A.; Oliveira, O.N. Langmuir monolayers of fractions of cork suberin extract. *Colloids Surf. B Biointerfaces* **2010**, *79*, 516–520. [CrossRef] [PubMed]
82. Deng, D.; Martin, S.T.; Ramanathan, S. Synthesis of hollow porous nanospheres of hydroxyl titanium oxalate and their topotactic conversion to anatase titania. *J. Mater. Res.* **2011**, *26*, 1545–1551. [CrossRef]
83. Li, K.; Wang, H.; Pan, C.; Wei, J.; Xiong, R.; Shi, J. Enhanced photoactivity of Fe + N Codoped anatase-rutile TiO₂ nanowire film under visible light irradiation. *Int. J. Photoenergy* **2012**, *1*, 398508.
84. Damkale, S.R.; Arbuj, S.S.; Umarji, G.G.; Rane, S.B.; Kale, B.B. Highly crystalline anatase TiO₂ nanocuboids as an efficient photocatalyst for hydrogen generation. *RSC Adv.* **2021**, *11*, 7587–7599. [CrossRef]
85. Masjedi, M.; Mir, N.; Noori, E.; Gholami, T.; Salavati-Niasari, M. Effect of Schiff base ligand on the size and the optical properties of TiO₂ nanoparticles. *Superlattices Microstruct.* **2013**, *62*, 30–38. [CrossRef]
86. Gholami, T.; Bazarganipour, M.; Salavati-Niasari, M.; Mir, N.; Hamadani, M.; Bagheri, S. Considering the effect of a ligand as new complexing agent in the characteristics of TiO₂ nanoparticles. *J. Mol. Liq.* **2016**, *215*, 467–471. [CrossRef]
87. Hidalgo, M.C.; Aguilar, M.; Maicu, M.; Navío, J.A.; Colón, G. Hydrothermal preparation of highly photoactive TiO₂ nanoparticles. *Catal. Today* **2007**, *129*, 50–58. [CrossRef]
88. Abenojar, J.; López de Armentia, S.; Barbosa, A.Q.; Martínez, M.A.; Velasco, F.; da Silva, L.F.M.; del Real Romero, J.C. Coating cork particles with iron oxide: Effect on magnetic properties. *Wood Sci. Technol.* **2020**, *54*, 869–889. [CrossRef]
89. Filipe-Ribeiro, L.; Cosme, F.; Nunes, F.M. Cork powder as a new natural and sustainable fining agent to reduce negative volatile phenols in red wine. *BIO Web Conf.* **2019**, *15*, 02017. [CrossRef]
90. Pereira, H.; Rosa, M.E.; Fortes, M.A. The Cellular Structure of Cork from *Quercus suber* L. *IAWA J.* **1987**, *8*, 213–218. [CrossRef]
91. Miranda, I.; Gominho, J.; Pereira, H. Cellular structure and chemical composition of cork from the Chinese cork oak (*Quercus variabilis*). *J. Wood Sci.* **2013**, *59*, 1–9. [CrossRef]
92. Oliveira, V. Cork Structural Characteristics and Their Influence on the Oxygen Ingress through Wine Stoppers. Ph.D. Thesis, Instituto Superior de Agronomia—Lisbon University, Lisbon, Portugal, 2016.
93. Pereira, H. The rationale behind cork properties: A review of structure and chemistry. *BioResources* **2015**, *10*, 6207–6229. [CrossRef]
94. Serra, P. Corticeira Amorim: Uncorking the Future. Master's Thesis, Católica Lisbon, Lisbon, Portugal, 2016.
95. Luisa, M.; Gioia, D.; Martins, L.M.; Pastor, I.M.; Khanam, S.; Rout, S.K. Enhanced Photocatalytic Oxidation of RhB and MB Using Plasmonic Performance of Ag Deposited on Bi₂WO₆. *Chemistry* **2022**, *4*, 272–296.

96. Zhao, J.; Wu, T.; Wu, K.; Oikawa, K.; Hidaka, H.; Serpone, N. Photoassisted degradation of dye pollutants.3. Degradation of the cationic dye rhodamine B in aqueous anionic surfactant/TiO₂ dispersions under visible light irradiation: Evidence for the Need of Substrate Adsorption on TiO₂ Particles. *Environ. Sci. Technol.* **1998**, *32*, 2394–2400. [[CrossRef](#)]
97. Maeno, K.; Patel, B.R.; Endo, T.; Kerman, K. Angle-sensitive photonic crystals for simultaneous detection and photocatalytic degradation of hazardous diazo compounds. *Micromachines* **2020**, *11*, 93. [[CrossRef](#)]
98. Rovisco, A. Solution-Based Zinc-Tin Oxide Nanostructures: From Synthesis to Applications. Ph.D. Thesis, FCT-UNL, Lisbon, Portugal, 2019.
99. Pintor, A.M.A.; Ferreira, C.I.A.; Pereira, J.C.; Correia, P.; Silva, S.P.; Vilar, V.J.P.; Botelho, C.M.S.; Boaventura, R.A.R. Use of cork powder and granules for the adsorption of pollutants: A review. *Water Res.* **2012**, *46*, 3152–3166. [[CrossRef](#)]
100. Bíbová, H.; Hykrdová, L.; Hoang, H.; Eliáš, M.; Jirkovský, J. SiO₂/TiO₂ composite coating on light substrates for photocatalytic decontamination of water. *J. Chem.* **2019**, *2019*, 2634398. [[CrossRef](#)]
101. Marques, A.V.; Rencoret, J.; Gutiérrez, A.; Del Río, J.C.; Pereira, H. Ferulates and lignin structural composition in cork. *Holz-forschung* **2016**, *70*, 275–289. [[CrossRef](#)]
102. Graça, J. Suberin: The biopolyester at the frontier of plants. *Front. Chem.* **2015**, *3*, 62. [[CrossRef](#)]
103. Andree, F.; Burkhardt, H.; Riedel, G. Rhodamine Dyes Which Are Sparingly Soluble or Insoluble in Water. U.S. Patent US3708499A, 2 January 1973.
104. Pintor, A.M.A.; Silvestre-Albero, A.M.; Ferreira, C.I.A.; Pereira, J.P.C.; Vilar, V.J.P.; Botelho, C.M.S.; Rodríguez-Reinoso, F.; Boaventura, R.A.R. Textural and surface characterization of cork-based sorbents for the removal of oil from water. *Ind. Eng. Chem. Res.* **2013**, *52*, 16427–16435. [[CrossRef](#)]
105. De Aguiar, T.R.; Guimarães Neto, J.O.A.; Şen, U.; Pereira, H. Study of two cork species as natural biosorbents for five selected pesticides in water. *Heliyon* **2019**, *5*, e01189. [[CrossRef](#)] [[PubMed](#)]
106. Zhang, J.; Zhou, P.; Liu, J.; Yu, J. New understanding of the difference of photocatalytic activity among anatase, rutile and brookite TiO₂. *Phys. Chem. Chem. Phys.* **2014**, *16*, 20382–20386. [[CrossRef](#)] [[PubMed](#)]
107. Lu, Y.; Zang, Y.; Zhang, H.; Zhang, Y.; Wang, G.; Zhao, H. Meaningful comparison of photocatalytic properties of {001} and {101} faceted anatase TiO₂ nanocrystals. *Sci. Bull.* **2016**, *61*, 1003–1012. [[CrossRef](#)]
108. Nunes, D.; Pimentel, A.; Gonçalves, A.; Pereira, S.; Branquinho, R.; Barquinha, P.; Martins, R. Metal Oxide Nanostructures for Sensor Applications. *Semicond. Sci. Technol.* **2019**, *34*, 043001. [[CrossRef](#)]
109. Bakbolat, B.; Daulbayev, C.; Sultanov, F.; Beissenov, R.; Umirzakov, A.; Mereke, A.; Bekbaev, A.; Chuprakov, I. Recent Developments of TiO₂-Based Photocatalysis in the Hydrogen Evolution and Photodegradation: A Review. *Nanomaterials* **2020**, *10*, 1790. [[CrossRef](#)]
110. Avilés-García, O.; Espino-Valencia, J.; Romero, R.; Rico-Cerda, J.L.; Natividad, R. Oxidation of 4-chlorophenol by mesoporous titania: Effect of surface morphological characteristics. *Int. J. Photoenergy* **2014**, *2014*, 210751. [[CrossRef](#)]
111. Li, G.; Lv, L.; Fan, H.; Ma, J.; Li, Y.; Wan, Y.; Zhao, X.S. Effect of the agglomeration of TiO₂ nanoparticles on their photocatalytic performance in the aqueous phase. *J. Colloid Interface Sci.* **2010**, *348*, 342–347. [[CrossRef](#)]
112. Wang, H.; Lewis, J.P. The reactive sites in faceted anatase nanoparticles. *Phys. Status Solidi B* **2011**, *248*, 2037–2043. [[CrossRef](#)]
113. Luttrell, T.; Halpegamage, S.; Tao, J.; Kramer, A.; Sutter, E.; Batzill, M. Why is anatase a better photocatalyst than rutile?—Model studies on epitaxial TiO₂ films. *Sci. Rep.* **2015**, *4*, 4043. [[CrossRef](#)]
114. El Mragui, A.; Logvina, Y.; Pinto da Silva, L.; Zegaoui, O.; Esteves da Silva, J.C.G. Synthesis of Fe- and Co-Doped TiO₂ with Improved Photocatalytic Activity Under Visible Irradiation Toward Carbamazepine Degradation. *Materials* **2019**, *12*, 3874. [[CrossRef](#)]
115. Colina-Márquez, J.; Machuca-Martínez, F.; Puma, G.L.; Mueses, M. Photocatalysis: Fundamentals, Materials and Potential. In *Molecules*; Pierre Pichat, Ed.; MDPI: Basel, Switzerland, 2016; pp. 1–664.
116. Alkaykh, S.; Mbarek, A.; Ali-Shattle, E.E. Photocatalytic degradation of methylene blue dye in aqueous solution by MnTiO₃ nanoparticles under sunlight irradiation. *Heliyon* **2020**, *6*, e03663. [[CrossRef](#)] [[PubMed](#)]
117. Gao, W.; Ran, C.; Wang, M.; Li, L.; Sun, Z.; Yao, X. The role of reduction extent of graphene oxide in the photocatalytic performance of Ag/AgX (X = Cl, Br)/rGO composites and the pseudo-second-order kinetics reaction nature of the Ag/AgBr system. *Phys. Chem. Chem. Phys.* **2016**, *18*, 18219–18226. [[CrossRef](#)]
118. Cogulet, A.; Blanchet, P.; Landry, V. Wood degradation under UV irradiation: A lignin characterization. *J. Photochem. Photobiol. B Biol.* **2016**, *158*, 184–191. [[CrossRef](#)]
119. De Vasconcelos, G.C.M.S.; De Carvalho, L.H.; Barbosa, R.; De Cássia De Lima Idalino, R.; Alves, T.S. Effects of weathering on mechanical and morphological properties cork filled green polyethylene eco-composites. *Polímeros* **2020**, *30*, e2020011. [[CrossRef](#)]
120. Badji, C.; Socalingame, L.; Garay, H.; Bergeret, A.; Bénézet, J.C. Influence of weathering on visual and surface aspect of wood plastic composites: Correlation approach with mechanical properties and microstructure. *Polym. Degrad. Stab.* **2017**, *137*, 162–172. [[CrossRef](#)]
121. Pandey, K.K. Study of the effect of photo-irradiation on the surface chemistry of wood. *Polym. Degrad. Stab.* **2005**, *90*, 9–20. [[CrossRef](#)]
122. Molinari, R.; Lavorato, C.; Argurio, P. Visible-Light Photocatalysts and Their Perspectives for Building Photocatalytic Membrane Reactors for Various Liquid Phase Chemical Conversions. *Catalysts* **2020**, *10*, 1334. [[CrossRef](#)]

123. Del Angel, R.; Durán-Álvarez, J.C.; Zanella, R. TiO₂-Low Band Gap Semiconductor Heterostructures for Water Treatment Using Sunlight-Driven Photocatalysis. In *Titanium Dioxide—Material for a Sustainable Environment*; IntechOpen: London, UK, 2018; pp. 1–518. ISBN 978-1-78923-327-8.
124. Lee, Y.J.; Lee, H.S.; Lee, C.G.; Park, S.J.; Lee, J.; Jung, S.; Shin, G.A. Application of PANI/TiO₂ Composite for Photocatalytic Degradation of Contaminants from Aqueous Solution. *Appl. Sci.* **2020**, *10*, 6710. [[CrossRef](#)]
125. Moulai, F.; Fellahi, O.; Messaoudi, B.; Hadjersi, T.; Zerroual, L. Electrodeposition of nanostructured γ -MnO₂ film for photodegradation of Rhodamine B. *Ionics* **2018**, *24*, 2099–2109. [[CrossRef](#)]
126. Zhang, K.; Yang, Y.; Xu, M.; Cheng, T.; Zhou, G. Synthesis of Mackinawite (FeSm) and its heterogeneous Fenton-like catalytic degradation performance of rhodamine B. *Water Sci. Technol.* **2022**, *85*, 354–366. [[CrossRef](#)]